

Partly burnt runaway stellar remnants from peculiar thermonuclear supernovae

R. Raddi,^{1*} M. A. Hollands,² D. Koester,³ J. J. Hermes,^{4,5} B. T. Gänsicke,² U. Heber,¹ K. J. Shen,⁶ D. M. Townsley,⁷ A. F. Pala,^{2,8} J. S. Reding,⁵ O. F. Toloza,² I. Pelisoli,⁹ S. Geier,⁹ N. P. Gentile Fusillo,² U. Munari,¹⁰ J. Strader¹¹

¹*Dr. Remeis-Sternwarte, Friedrich Alexander Universität Erlangen-Nürnberg, Sternwartstr. 7, 96049 Bamberg, Germany*

²*University of Warwick, Department of Physics, Gibbet Hill Road, Coventry, CV4 7AL, United Kingdom*

³*Universität Kiel, Institut für Theoretische Physik und Astrophysik, 24098, Kiel, Germany*

⁴*Department of Astronomy, Boston University, 725 Commonwealth Ave., Boston, MA 02215, US*

⁵*University of North Carolina, Department of Physics and Astronomy, Chapel Hill, NC - 27599-3255, US*

⁶*Department of Astronomy and Theoretical Astrophysics Center, University of California, Berkeley, CA 94720, USA*

⁷*University of Alabama, Department of Physics and Astronomy, Tuscaloosa, AL, USA*

⁸*European Southern Observatory, Karl-Schwarzschild-Str. 2, 85748, Garching*

⁹*Institut für Physik und Astronomie, Universität Potsdam, Haus 28, Karl-Liebknecht-Str. 24/25, D-14476 Potsdam-Golm, Germany*

¹⁰*INAF-Astronomical Observatory of Padova, I-36012 Asiago*

¹¹*Department of Physics and Astronomy, Michigan State University, East Lansing, MI 48824, USA*

Accepted 2019 June 06. Received 2019 May 08; in original form 2019 February 13

ABSTRACT

We report the discovery of three stars that, along with the prototype LP 40–365, form a distinct class of chemically peculiar runaway stars that are the survivors of thermonuclear explosions. Spectroscopy of the four confirmed LP 40–365 stars finds O/Ne-dominated atmospheres enriched with remarkably similar amounts of nuclear ashes of partial O- and Si-burning. Kinematic evidence is consistent with ejection from a binary supernova progenitor; at least two stars have rest-frame velocities indicating they are unbound to the Galaxy. With masses and radii ranging between 0.20–0.28 M_{\odot} and 0.16–0.60 R_{\odot} , respectively, we speculate these inflated white dwarfs are the partly burnt remnants of either peculiar Type Ia_x or electron-capture supernovae. Adopting supernova rates from the literature, we estimate that ~ 20 LP 40–365 stars brighter than 19 mag should be detectable within 2 kpc from the Sun at the end of the *Gaia* mission. We suggest that as they cool, these stars will evolve in their spectroscopic appearance, and eventually become peculiar O-rich white dwarfs. Finally, we stress that the discovery of new LP 40–365 stars will be useful to further constrain their evolution, supplying key boundary conditions to the modelling of explosion mechanisms, supernova rates, and nucleosynthetic yields of peculiar thermonuclear explosions.

Key words: star: individual: LP 40–365 — supernova: general — white dwarfs — subdwarfs — Galaxy: kinematics and dynamics

1 INTRODUCTION

LP 40–365 (GD 492; Luyten 1970; Giclas et al. 1970) is a high-velocity star unbound to the Galaxy with a unique composition: it has an O/Ne-dominated atmosphere sprinkled with the ashes of incomplete O- and Si-burning (Vennes et al. 2017). These authors have proposed LP 40–365 as a partially burnt runaway white dwarf that survived disruption by a thermonuclear supernova,

specifically a peculiar group that is suggested to experience pure deflagrations, leading to subluminal explosions that do not completely disrupt the white dwarf accretors (SN 2002cx-like, or SNe Ia_x; Li et al. 2003; Phillips et al. 2007; Jordan et al. 2012; Foley et al. 2013; Kromer et al. 2013, 2015; Fink et al. 2014; Jha 2017). In Raddi et al. (2018b), hereafter Paper I, we presented supportive evidence for the formation of LP 40–365 in a single-degenerate thermonuclear supernova by measuring a super-solar Mn abundance that is compatible with theoretical nucleosynthesis yields of near-Chandrasekhar-mass (M_{Ch}) explosions

* E-mail: roberto.raddi@fau.de

(Seitenzahl et al. 2013; Seitenzahl & Townsley 2017), and it is also in agreement with the hypothesis of LP 40–365 as SN Iax survivor (Vennes et al. 2017).

In Raddi et al. (2018a), hereafter *Paper II*, we used the precise parallax available in the Second *Gaia* Data Release (*Gaia* DR2; Gaia Collaboration et al. 2018) to estimate the radius of LP 40–365 to be $R \approx 0.18 R_{\odot}$, i.e. one order of magnitude larger than canonical white dwarf radii (Tremblay et al. 2017). We interpreted this finding with the star being currently inflated as a consequence of the supernova explosion (Jordan et al. 2012; Kromer et al. 2013; Shen & Schwab 2017). The scenario of a post-explosion expansion is compatible with the low rotational velocity of the star ($v \sin i \leq 50 \text{ km s}^{-1}$; Vennes et al. 2017, *Paper I*). Studying the kinematics of LP 40–365, we demonstrated it is gravitationally unbound from the Milky Way (see also Vennes et al. 2017), having a rest frame velocity of $v_{\text{rf}} \approx 850 \text{ km s}^{-1}$ that is about 1.5 times larger than the escape velocity at the corresponding Galactocentric radius. Considering that LP 40–365 has benefitted from the Galactic rotation, we estimated it gained an ejection velocity of $\approx 600 \text{ km s}^{-1}$ at the moment of the supernova explosion. In the single-degenerate scenario, considering negligible contribution from asymmetric mass loss, this velocity could be achievable via the ejection from a compact binary (1 hr orbital period), e.g. with a massive He-burning companion (Wang & Han 2009; Wang et al. 2013).

Among many exciting discoveries, *Gaia* DR2 has led to another possible breakthrough in the field of thermonuclear supernova research with the identification of three new hyper-runaways with $v_{\text{rf}} \gtrsim 1000 \text{ km s}^{-1}$ (Shen et al. 2018b). These stars form a new, relatively homogeneous spectral class of subluminescent, CO-rich objects likely connected to the explosion mechanism of supernovae Type Ia (SN Ia) that is known as *dynamically driven double-degenerate double-detonation* scenario (D^6 ; Shen et al. 2018a).

LP 40–365 is interpreted as the formerly accreting white dwarf in a single-degenerate mass-transferring binary (Vennes et al. 2017), also referred to as the bound remnant. On the other hand, the D^6 stars are interpreted as the former compact donors in close, double-degenerate binaries. Also the D^6 stars are suggested to have reached their rest-frame velocities by conserving their high orbital velocities at the moment of explosion. Like LP 40–365, the D^6 stars are currently thermally bloated; however, their expansion might be caused by the pre-explosion tidal forces and the interaction with the supernova ejecta (Shen & Schwab 2017). Prior to *Gaia* DR2, a hyper-runaway He-rich subdwarf star, US 708 (Hirsch et al. 2005; Heber 2016), was proposed as the fastest known star that may have been the former subdwarf donor in a thermonuclear supernova event (Justham et al. 2009; Geier et al. 2015). Following the identification of the D^6 stars, Shen et al. (2018b) have suggested a connection with US 708, which they proposed as representative for a possible later stage on the way back towards the canonical white dwarf cooling sequence. All together, LP 40–365, the D^6 stars, and US 708 likely represent the first direct evidence of a wider class of binary progenitors for thermonuclear supernovae (Wang & Han 2012; Maoz et al. 2014).

We have performed spectroscopic follow-up of candidate high-velocity stars, which we selected by mining *Gaia* DR2. Our search has successfully led to the identification

of two additional stars that, along with LP 40–365, we propose to form a distinct class of partly burnt, post-supernova runaway stars (hereafter, “LP 40–365 stars”). Furthermore, by mining the Sloan Digital Sky Survey (SDSS) spectroscopic database (Smee et al. 2013; Abolfathi et al. 2018), we have identified two related objects: one is very likely also an LP 40–365 star, while the other requires further follow-up observations.

In this manuscript, we present follow-up observations of the *Gaia* candidates, and the identification of the SDSS candidates. In Section 3, we detail the spectral analysis¹ of the LP 40–365 stars identified with *Gaia*, and we re-analyse LP 40–365 itself including new *Hubble Space Telescope* (*HST*) near-ultraviolet (NUV) spectroscopy. We present the Galactic orbits of the new LP 40–365 stars in Section 4. In Section 5, we discuss our results in a broader context, focusing on: i) the chemical composition, compared to theoretical simulations of white dwarfs that are predicted to survive peculiar thermonuclear explosions; ii) physical parameters (mass and radius); iii) evolutionary status, drawing a comparison with theoretical predictions; and iv) kinematics, birth places and binary progenitors. Finally, in Section 5.2, we model a population of LP 40–365 stars to estimate the end-of-mission detection limits of *Gaia* within 2 kpc from the Sun, deriving the distribution of astrometric parameters. In our conclusions, we summarise the remarkable similarities among the observed stars.

2 OBSERVATIONS

2.1 *Gaia* DR2 selection

We searched for high-velocity-star candidates by selecting *Gaia* objects having relatively large transverse velocities ($v_t \gtrsim 300 \text{ km s}^{-1}$) and falling within the extended colour space below the main sequence in the *Gaia* colour-magnitude Hertzsprung-Russell (HR) diagram (Fig. 1) that is occupied both by LP 40–365 and the D^6 stars, i.e. delimited by *Gaia* colours of $B_p - R_p \lesssim 0.7$ and absolute magnitudes of $M_G \gtrsim 2.5$. Limiting the parallax precision to $\varpi/\sigma_{\varpi} > 5$, our criteria included LP 40–365 and D^6 –2, but excluded the two other D^6 stars. The spectroscopic follow-up has led to the identification of several canonical hot subdwarfs and white dwarfs, which we will present elsewhere. Two stars stood out – *Gaia* DR2 5822236741381879040 and *Gaia* DR2 6727110900983876096 (hereafter shortened to J1603–6613 and J1825–3757, respectively, based on their equatorial coordinates) – as possessing peculiar spectra, clearly resembling that of LP 40–365 (see Fig. 2). J1603–6613 was previously unknown, while we previously obtained a low-resolution spectrum of J1825–3757 (Fig. 2) on the base of which we had classified it as a likely hot subdwarf (Raddi et al. 2017). Follow-up observations are detailed in the next sections, and the journal of observations is listed in Table 2. The *Gaia* DR2 astrometry and photometry of the new stars are listed in Table 1.

J1603–6613 has an apparent magnitude $G = 17.84$ that,

¹ The spectra analysed here are made available at the Open Fast Star Catalogue (<https://faststars.space/>), which is currently maintained by Douglas Boubert and James Guillochon.

Table 1. Astrometric and photometric parameters of J1603–6613 and J1825–3757, including broad-band photometry from *GALEX* (NUV; Morrissey et al. 2007), SkyMapper (*uvgriz*; Wolf et al. 2018), and Vista Hemisphere Survey (*J*; McMahon et al. 2013).

Parameters	Symbols	J1603–6613	J1825–3757
Designation		Gaia DR2 5822236741381879040	Gaia DR2 6727110900983876096
Right Ascension [hms]	α	16:03:04.06	18:25:22.15
Declination [dms]	δ	−66:13:26.9	−37:57:26.1
Galactic longitude [deg]	ℓ	320.63	356.03
Galactic latitude [deg]	b	−10.18	−11.58
Parallax [mas]	ϖ	0.57 ± 0.10	1.08 ± 0.06
Proper motions [mas yr ^{−1}]	$\mu_\alpha \cos \delta$	$+39.8 \pm 0.1$	$−37.6 \pm 0.1$
	μ_δ	$−7.1 \pm 0.2$	$−143.0 \pm 0.1$
Fluxes [mag]	G	17.84	13.28
	B_p	17.89	13.21
	R_p	17.75	13.26
	NUV	20.19 ± 0.22	14.61 ± 0.01
	u	17.985 ± 0.031	13.251 ± 0.002
	v	17.829 ± 0.082	13.227 ± 0.009
	g	17.691 ± 0.062	13.214 ± 0.006
	r	17.831 ± 0.030	13.317 ± 0.002
	i	18.126 ± 0.064	13.609 ± 0.003
	z	–	13.799 ± 0.002
	J	17.667 ± 0.057	13.288 ± 0.002

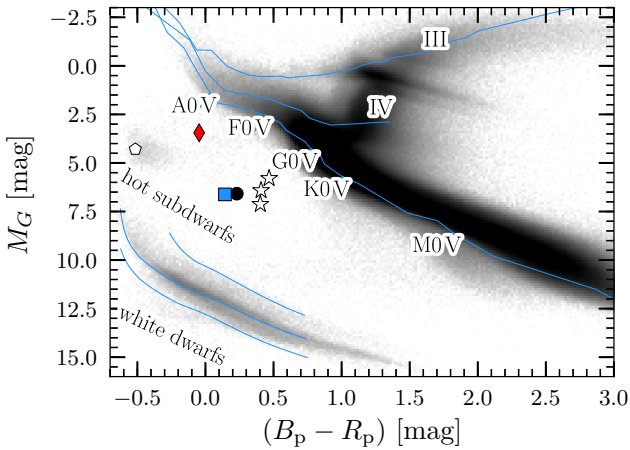


Figure 1. *Gaia* HR diagram. LP 40–365, J1603–6613, and J1825–3757 are shown as circle, square, and diamond symbols, respectively (correspondence between colours and symbols will be maintained in the following figures). The three D⁶ objects, identified by Shen et al. (2018b), are marked by star-shaped symbols. US 708, for which we adopt a spectroscopic distance of 8.5 ± 1.0 kpc (Geier et al. 2015), is plotted as a pentagon symbol. Error bars are smaller or of the order of the symbol sizes. The intrinsic colours of normal stars are interpolated from the Pickles (1998) spectral library (luminosity class V, III, I). Cooling tracks for 0.2, 0.6, 1.0 M_\odot white dwarfs (from top to bottom) are derived by scaling a grid of synthetic spectra in the $T_{\text{eff}} = 6000$ –90,000 K range (Koester 2010) with standard mass-radius relations for pure-hydrogen atmospheres (Wood 1995; Bergeron et al. 2001; Fontaine et al. 2001) and convolving them with the *Gaia* DR2 filter profiles.

combined with its parallax $\varpi = 0.57 \pm 0.10$ mas, corresponds to an absolute magnitude $M_G = 6.62$, which is similar to that of LP 40–365. This new star is slightly bluer than LP 40–365, suggesting it may be hotter. The *Gaia* colour excess factor $(f_{BP} + f_{RP})/f_G = 1.6$ might indicate some prob-

lems with the photometry, given that the star is observed in a relatively crowded field. We note an interstellar extinction in the V-band $A_V = 0.28$ –0.32 (Schlegel et al. 1998; Schlafly & Finkbeiner 2011), i.e. about four times larger than the that along the LP 40–365 sightline.

J1825–3757 is located closer to the Sun, having a parallax of $\varpi = 1.08 \pm 0.06$ mas. It is intrinsically bluer and about 3 mag brighter than LP 40–365 and J1603–6613, implying it is both hotter and larger than the other two stars. The total interstellar extinction is comparable to that of J1603–6613.

2.2 J1603–6613

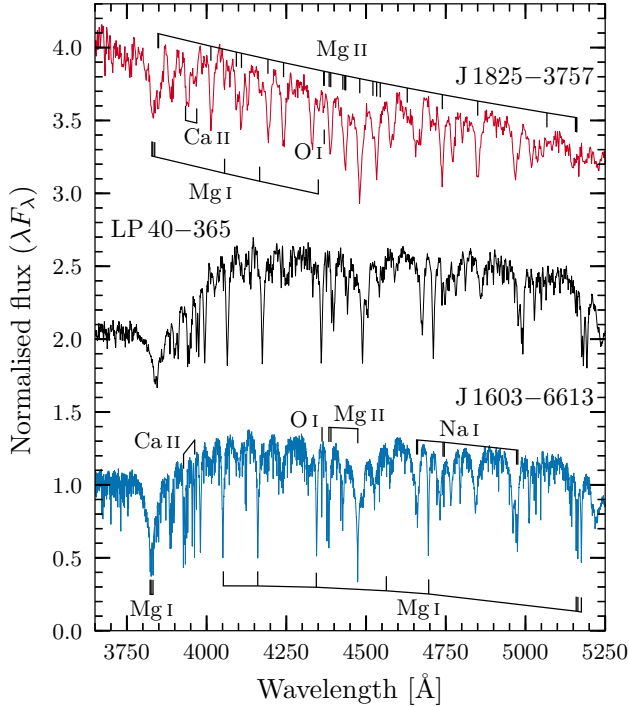
2.2.1 Low-resolution spectroscopy

We first observed J1603–6613 on 2018 May 6 with the Goodman Spectrograph (Clemens et al. 2004) mounted on the 4.1 m Southern Astrophysical Research (SOAR) telescope at Cerro Pachón in Chile. We obtained 8×300 s consecutive spectra using a 930 line/mm grating with wavelength coverage between 3600–5200 Å. We used a 1''01 slit and bracketed our exposures with a 60 s Fe arc lamp, since no skylines exist in this spectral region for wavelength calibration. With a dispersion of 0.84 Å/pixel our resolution is roughly 2.8 Å.

The spectra were optimally extracted (Horne 1986) using standard STARLINK routines (Currie et al. 2014), after applying bias and quartz-lamp flat corrections using the software PAMELA. We used the software package MOLLY (Marsh 1989) to wavelength calibrate the spectra, apply a heliocentric correction, and perform a final weighted average of the one-dimensional (1D) spectra, and used the spectrophotometric standard EG 274 for flux calibration. We did not detect any radial velocity shift between the exposures, within the precision of the wavelength calibration, and thus coadded all spectra to obtain a spectrum with a signal-to-noise ratio of $S/N \approx 20$ per pixel, shown in Fig. 2. Noting the striking similarity with LP 40–365, we used the strongest lines to estimate the radial velocity with respect to the Sun via

Table 2. Observing logs of the data presented and analysed in this work.

Mode	Instrument	LP 40–365	J1603–6613	J1825–3757
Spectroscopy	SOAR/Goodman		2018 May 6	
	VLT/X-shooter		2018 Jul 9	2016 Sep 27
	<i>HST</i> /STIS	2018 May 21, 25		
Photometry	SOAR/Goodman		2018 May 10	2018 Jul 8

**Figure 2.** Comparison between the new stars and LP 40–365, with some of the strongest lines labelled. The NTT/EFOSC2 spectrum of J1825–3757 (Raddi et al. 2017) and the SOAR/Goodman spectrum of J1603–6613 have a resolution of ≈ 8 and 2.8 \AA , respectively. The WHT/ISIS spectrum of LP 40–365 from Paper I has a 2 \AA resolution. All the spectra are plotted in the heliocentric frame, so spectral lines are shifted by the radial velocity of each star.

cross correlation with our synthetic model of LP 40–365, obtaining $v_{\text{rad}} = -480 \pm 10 \text{ km s}^{-1}$ that confirmed J1603–6613 as a high-velocity star.

2.2.2 Intermediate-resolution spectroscopy

We followed up J1603–6613 again on 2018 July 9, with the multi-wavelength intermediate-resolution spectrograph X-shooter (Vernet et al. 2011), mounted at the Cassegrain focus of the ESO Very Large Telescope (VLT) UT2 in Cerro Paranal (Chile). We binned the detectors (1×2 in the spatial and dispersion directions, respectively) and we used narrow slits of $1''.0$, $0''.9$, and $0''.9$, in the UVB, VIS, and NIR arms, respectively, taking six exposures in each arm and achieving total exposure times of 7320, 7500, and 7800 s, in order to reduce the impact of cosmic rays and to confirm the absence of radial-velocity variability. The mean seeing was of $0''.6$.

The data were reduced using the standard ESO pipeline

Reflex (Freudling et al. 2013), and the *molecfit* software (Smette et al. 2015; Kausch et al. 2015) was used to remove the telluric absorption of Earth’s atmosphere. Again, we did not observe any significant radial-velocity variation over short timescales, so we coadded the individual exposures to obtain an average spectrum, confirming the same blue-shifted radial velocity. The coadded spectrum has a $S/N \sim 100$ in the blue/visual spectral range, with resolving power $R = 5400$, 8900, and 5600, in the UVB, VIS, and NIR arms, respectively.

2.2.3 Time-series photometry

We performed time-series photometry of J1603–6613 on the night of 2018 May 10 using the imaging mode of the Goodman spectrograph on SOAR. We used an exposure time of 17 s and had a readout time of 2.0 s, and observed for 2.7 hr through a *S8612* broad-bandpass, red-cutoff filter (3300–6200 Å). Seeing across the duration of the observation was fairly stable, averaging $1''.1$ – $1''.5$.

Images were debiased and flat-fielded using an internal dome lamp. We extracted a light curve using standard circular aperture photometry, with a 4.5-px aperture surrounded by an 8-px annulus. The target light curve was normalised using a bright, nearby comparison star with no close companions, and we subtracted out a second-order polynomial to account for airmass changes. A Lomb-Scargle periodogram showed no significant peaks above 0.2 per cent amplitude for periods between roughly 40–4000 s. This lack of variability suggests that J1603–6613, like LP 40–365, is consistent with not-having an unseen close companion.

2.3 J1825–3757

2.3.1 Intermediate-resolution spectroscopy

In Raddi et al. (2017) we published a low-resolution spectrum (8 \AA) of J1825–3757 taken at the New Technology Telescope with the ESO Faint Object Spectrograph and Camera v.2 (NTT/EFOSC2; Buzzoni et al. 1984) at the La Silla observatory (shown in Fig. 2). Although we classified this star as a likely hot subdwarf, its spectrum shows numerous unusually strong Mg I–II lines and other ionised metals. The absence of H and He lines resembles the spectral appearance of LP 40–365 and J1603–6613.

We followed up J1825–3757 on 2016 September 27 with VLT/X-shooter, taking single exposures of 521, 550, and 600 s in the blue, visual, and near-infrared arms, respectively. The instrument setup and data reduction steps were the same as those adopted for J1603–6613. The mean seeing during the observations of J1825–3757 was $0''.7$. The achieved resolving power were 4300, 7400, and 5400, in the

UVB, VIS, and NIR, respectively. The extracted spectrum has a S/N > 150 in the UVB/VIS arms and > 100 in the NIR arm.

2.3.2 Time-series photometry

We also observed J1825–3757 through a Bessel-V filter on the night of 2018 July 08 with the imaging mode of the Goodman spectrograph on SOAR. We collected 1140×5 s exposures, and each exposure had roughly 2.0 s of dead time from readout. Seeing was steady from $1''.6$ – $1''.7$. As with J1603–6613 we bias- and flat-field corrected the photometry and extracted the light curve using a fixed 5.5 px circular aperture, and subtracted a second-order polynomial to account for airmass changes throughout the 2.2 hr run. We did not see any coherent variability at any period from 15–3500 s, to a limit of at least 0.1 per cent amplitude, consistent with it currently being an isolated star.

2.4 LP 40–365

2.4.1 HST spectroscopy

We observed LP 40–365 with *HST* using the Space Telescope Imaging Spectrograph (STIS; Woodgate et al. 1998) on 2018 May 21 and 25, during Cycle 25, for three and two orbits, respectively. The total exposure time amounted to 15 253 s. We used the G230L grating and the NUV Multianode Microchannel Array (MAMA) detector with a $52'' \times 2''$ aperture, which delivers a resolving power $R \approx 1000$ across the 1570–3180 Å wavelength range. We applied the wavelength and flux calibration via standard IRAF CALSTIS tasks (Katsanis & McGrath 1998). We measured an average S/N ≈ 35 from the reduced spectrum.

2.5 SDSS spectra

We also considered the possibility that similar stars may reside within the 4.9 million spectra of the SDSS database (Abolfathi et al. 2018), which could have been previously misclassified due to their unusual spectral features.

We adapted the template method of Hollands et al. (2017), which essentially fits all SDSS spectra against a library of spectral templates. We created a grid of synthetic LP 40–365 spectra, i.e. with T_{eff} ranging from 5000 to 7000 K in steps of 500 K, and then up to 20 000 K in steps of 1000 K. In all cases the log g was fixed at 5 dex, and the abundances fixed to the average of the already identified stars (as justified by the results presented in Section 3). For each model, additional spectral templates were offset by fixed radial-velocity shifts ranging from -1500 to $+1500 \text{ km s}^{-1}$, in steps of 50 km s^{-1} , resulting in a total of 1098 templates. Finally, we convolved each template with a Gaussian to match the SDSS spectral resolution of 2.7 Å . To filter other easily identifiable spectral types, we complemented the grid of LP 40–365 templates with 1843 white dwarf templates (spectral classes DA, DB, DZ), and 1045 stellar templates of spectral types commonly observed by SDSS (see description in Hollands et al. 2017). For each SDSS spectrum, we interpolated all templates onto the SDSS wavelength scale, flux-scaled them to the data, and then evaluated their χ^2 , adopting the template with the lowest

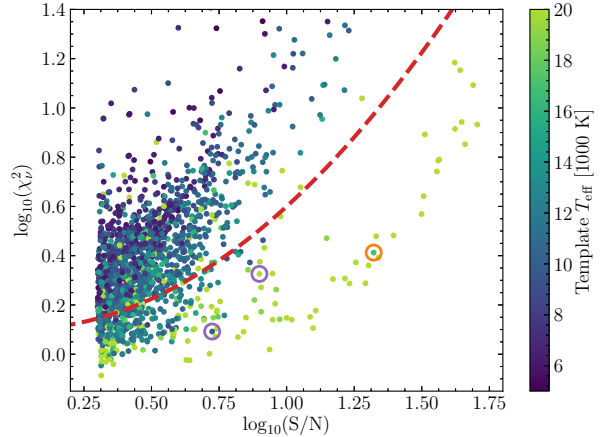


Figure 3. χ^2_v vs. spectral S/N for SDSS spectra that match best to an LP 40–365 template. The red dashed curve indicates a cut, below which the corresponding spectra were visually inspected. Two new candidates are circled in purple, whereas J1240+6710 is circled in orange.

χ^2 as the best match. The scaling factor was the only free-parameter, whose optimal value was determined analytically (see eq. 1 in Hollands et al. 2017). The closest-matching template, the corresponding reduced χ^2 (χ^2_v), and the mean spectral signal-to-noise (S/N) between 4500–6000 Å were recorded for each SDSS spectrum.

Out of the 3.1 million SDSS spectra with a mean S/N > 2, 1544 were best matched by a LP 40–365 model. Even so, a closest match did not guarantee a good fit. In Figure 3, we show the χ^2_v of the best-matching templates vs. the SDSS spectrum mean S/N, with the template- T_{eff} indicated by the point-colours. Towards high S/N, the distribution in χ^2_v becomes bimodal. Points in the upper-branch correspond to spectra where all templates provided poor matches, but with one of the LP 40–365 templates as the least bad. The lower-branch corresponds to more convincing matches to the templates. Notably, most of the points in the lower branch correspond to high- T_{eff} templates, as their metal-lines become weaker, and thus the number of false-positives increases. The red-dashed line indicates our cut in the χ^2_v -S/N plane. The spectra corresponding to the 349 objects below the cut were visually inspected and compared with their best fitting templates.

Following this visual inspection, three spectra showed convincing resemblance to their templates. One of these (Fig. 3, circled in orange) is the O-dominated atmosphere white dwarf (DOx), SDSS J124043.00+671034.6 (hereafter J1240+6710; Kepler et al. 2016), where matches to Mg, O, and Si lines resulted in a favourable χ^2_v . The other two objects (Figure 3, circled in purple) are SDSS J090535.55+251011.3 and SDSS J163712.21+363155.9, (hereafter J0905+2510 and J1637+3631 respectively). The spectra of the two SDSS candidates, with their best-matching templates, are shown in Figure 4. Their astrometry and photometry are provided in Table 3.

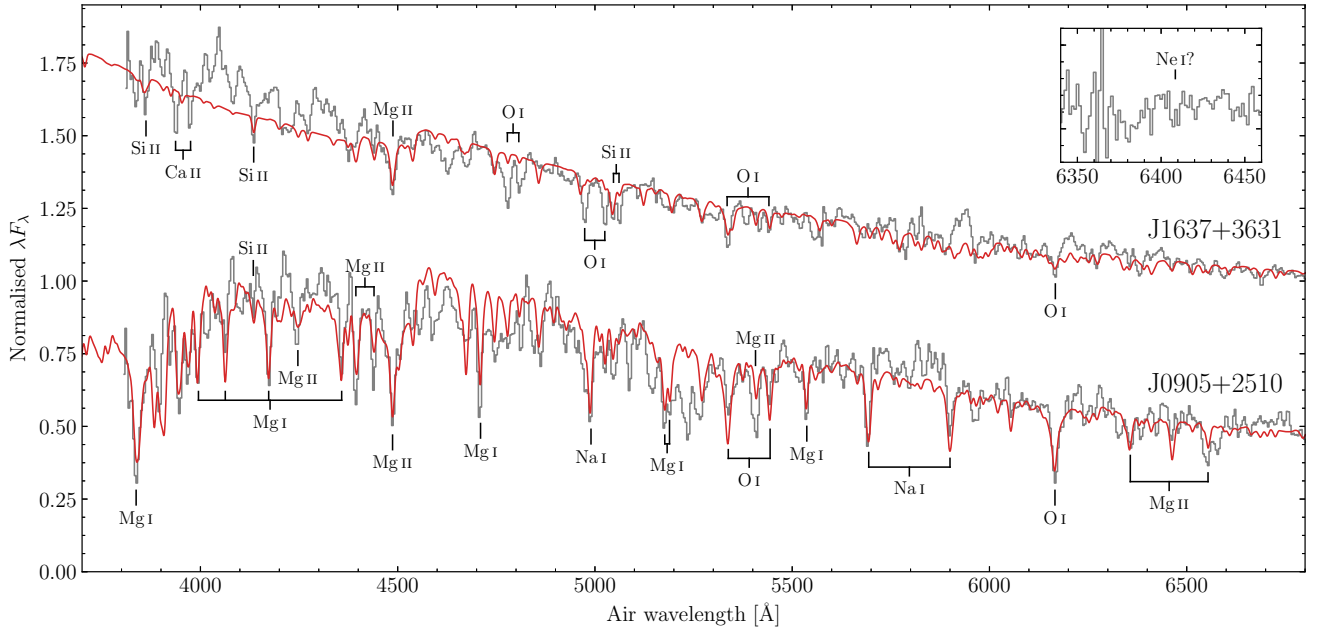


Figure 4. Normalised SDSS spectra of J0905+2510 (bottom) and J1637+3631 (top, offset by +0.75). Their best matching “LP 40–365 star” templates are shown in red. For clarity, the spectra and templates have been convolved by Gaussians of FWHM = 8 Å to better show the strongest transitions (labelled). For J1637+3631, an inset shows a tentative Ne I detection (at the nominal SDSS resolution). Both spectra are shown in the heliocentric frame.

Table 3. Astrometry, photometry, and spectroscopic parameters for the objects identified from SDSS spectra, J0905+2510 and J1637+3631. Reddening values were determined from the Pan-STARRS dust-maps (Chambers et al. 2016; Green et al. 2018). Photometric T_{eff} were calculated from fitting our “LP 40–365 star” models to the GALEX NUV and SDSS photometry including the quoted reddening. Results from our template matching are given at the bottom.

Parameter [units]	Symbol	J0905+2510	J1637+3631
Gaia Designation		Gaia DR2 688380457507044864	Gaia DR2 1327920737357113088
Right Ascension [hms]	α	09:05:35.55	16:37:12.21
Declination [dms]	δ	+25:10:11.3	+36:31:55.9
Galactic longitude [deg]	ℓ	201.65	58.98
Galactic latitude [deg]	b	+39.71	+41.82
Parallax [mas]	ϖ	–	0.39 ± 0.60
Proper motions ¹ [mas yr ^{−1}]	$\mu_{\alpha} \cos \delta$	3.1 ± 3.4	-18.5 ± 1.2
	μ_{δ}	24.7 ± 3.0	$+64.2 \pm 1.2$
Fluxes [mag]	G	19.62	20.33
	B_p	19.69	20.19
	R_p	19.36	20.21
	NUV	22.23 ± 0.28	20.44 ± 0.17
	u	20.26 ± 0.05	20.01 ± 0.05
	g	19.67 ± 0.01	20.09 ± 0.02
	r	19.73 ± 0.02	20.40 ± 0.04
	i	19.96 ± 0.03	20.62 ± 0.06
	z	20.03 ± 0.12	20.86 ± 0.28
Interstellar reddening [mag]	$E(B - V)$	0.0 ± 0.02	0.02 ± 0.02
Photometric temperature [K]	T_{eff}	$10\,050 \pm 140$	$13\,500 \pm 600$
Template parameters	T_{eff} [K]	10 000	20 000
	RV [km s ^{−1}]	+300	+300
	χ^2_{ν}	1.24	2.12
Spectrum S/N		5.30	7.93
Plate-MJD-fiber		2086-53401-0500	2185-53532-0360

Notes: ¹The proper motions of J0905+2510 are taken from the Pan-STARRS–SDSS cross-match (Tian et al. 2017).

2.5.1 J0905+2510

With a mean S/N of 5.3, a cursory inspection of the SDSS spectrum of J0905+2510 simply appears as a noisy black-body. However, degrading the resolution to 8 \AA (Figure 4, bottom) reveals lines of O I, Na I, Mg I/II, and Si II. The close agreement between the strong lines in the data and best-matching template indicates that this star also belongs to the class of “LP 40–365 stars.” We also note some discrepancy near 5230 \AA , corresponding to a feature, currently not accounted for by the models, that is also observed in LP 40–365 as well as in J1603–6613 and LP 40–365 which Vennes et al. (2017) attributed to a resonance in the photoionisation cross-section of Mg.

J0905+2510 has only a two-parameter astrometric solution (position) within the *Gaia* DR2 data. With $G = 19.62$, it is probable that a parallax will be available in a future *Gaia* data release. Assuming J0905+2510 has an absolute G magnitude similar to LP 40–365 and J1603–6613 (6.5 mag), the true distance is likely to be about 4 kpc from the Sun. Given the proper motion of $(\mu_\alpha \cos \delta, \mu_\delta) = (3.1 \pm 3.4, 24.7 \pm 3.0) \text{ mas yr}^{-1}$ (Tian et al. 2017), the implied transverse velocity is about 500 km s^{-1} , which is broadly consistent with the 300 km s^{-1} radial velocity.

To more accurately measure the T_{eff} , we fitted our LP 40–365 model grid to *GALEX* NUV and SDSS photometry (interpolating amongst models for estimating intermediate T_{eff} to our grid-steps). We accounted for interstellar reddening, $E(B - V) = 0.04 \pm 0.02 \text{ mag}$, (as estimated via the Pan-STARRS 3D dust-maps at a heliocentric distance of at 4 kpc; Green et al. 2018), obtaining $9840 \pm 170 \text{ K}$. A full abundance analysis and comparison with the other members of this class necessitates higher-quality follow-up spectra.

2.5.2 J1637+3631

This star was first reported as a white dwarf with a C-rich, He-dominated atmosphere (DBQ spectral type) in the SDSS DR7 white dwarf catalogue of Kleinman et al. (2013). However, we neither see evidence for He nor C features. Beyond the general Rayleigh-Jeans slope, the main spectral features matched by the template (Figure 4, top) are the 4129 \AA Si II and 4481 \AA Mg II lines (rest wavelengths), although redshifted by about 300 km s^{-1} . Transitions from O I and Ca II appear stronger than in the template, indicating somewhat different abundances than assumed for our grid of models. The 6402 \AA Ne I line is also tentatively detected in the unsmoothed SDSS spectrum (Figure 4, inset).

For J1637+3631, *Gaia* DR2 provides a full five-parameter astrometric solution, although rather poorly constrained. With a parallax of $0.39 \pm 0.60 \text{ mas}$, we place a 3σ lower limit of about 500 pc on the distance. The implied absolute magnitude is $M_G = 11.8$. Applying a smooth exponentially decreasing prior that accounts for the stellar density distribution in the Milky Way, Bailer-Jones et al. (2018) have estimated a distance of $d = 1550^{+1115}_{-630} \text{ pc}$, which implies an intrinsic magnitude of $M_G = 9.3 \pm 1.2$. Both these distance estimates place J1637+3631 within the white dwarf sequence of Figure 1.

Of course J1637+3631 could be much further away and still remain consistent with the *Gaia* parallax. If we assume J1637+3631 is a LP 40–365 star, and conservatively,

like LP 40–365 itself, has $M_G = 6.5$, the implied distance would be about 6 kpc. Given the 67 mas yr^{-1} proper-motion (Table 3), the transverse velocity would be $\sim 2000 \text{ km s}^{-1}$ – several times larger than theoretical predictions for SNe Ia survivors (Shen et al. 2018b).

Hence, a more likely explanation is that J1637+3631 could be the second representative of the DOx white dwarf class, after J1240+6710 (Kepler et al. 2016). This hypothesis can be tested with medium-resolution follow-up spectroscopy. One difference we note between these two stars is the intensity of the Ca II H+K lines: they are plainly visible in the spectrum of J1637+3631, but only an upper-limit of Ca was determined for J1240+6710. Our photometric T_{eff} , determined from fitting *GALEX* and SDSS photometry ($13500 \pm 600 \text{ K}$, Table 3), is cooler than the $21590 \pm 620 \text{ K}$ measured by Kepler et al. (2016) for J1240+6710, which could explain the differences in Ca II strength.

3 SPECTRAL ANALYSIS

3.1 J1603–6613

Fig. 2 shows that J1603–6613 has a spectrum remarkably similar to LP 40–365, thus providing a natural starting point for the spectral analysis. Owing to the high S/N and resolution of the X-shooter spectrum, we searched for lines from other elements in addition to those previously identified in LP 40–365. We identified new lines from Sc II, Co I–II, Zn I, Cu I, and Sr II. C I lines were also found to be present at optical wavelengths. As with LP 40–365, no evidence for H or He were seen, but with more stringent limits from the much higher S/N ratio and $\simeq 1000 \text{ K}$ hotter T_{eff} .

We precisely measured the blue-shift of J1603–6613 by fitting Lorentzian profiles to some of the strong, isolated O I and Mg I lines in the VIS arm of the X-shooter spectrum, obtaining $v_{\text{rad}} = -485 \pm 4 \text{ km s}^{-1}$, which confirms the estimate from the identification spectrum.

As previously noted in Paper I for LP 40–365, a hotter T_{eff} clashes with the non-detection of He I absorption at 5877 \AA . Given the similarity between the two stars, we reconsidered the feasibility of a ONe-dominated atmosphere, as found by Vennes et al. (2017) for LP 40–365. Our model spectra were computed following the methods of Koester (2010), as already done in Paper I. We have made use of the most recent atomic data². One important result is that also ONe-atmospheres develop relatively deep convection zones ($\sim 10^{-6} M_{\text{star}}$), which extend down to the bottom of the model atmosphere like for He-dominated atmospheres in the same temperature range. Although we could not estimate the size of the mixing zone below the atmosphere, we have estimated the diffusion timescales of the detected elements

² The most relevant updates for the current project include new oscillator strengths and broadening constants from the atomic line databases NIST (National Institute of Standards and Technology; Kramida et al. 2019), VALD (Vienna Atomic Line Data; Ryabchikova et al. 2015; Kupka et al. 2000), and Robert Kurucz’s line lists for O I and Mg II (<http://kurucz.harvard.edu/>). Also new is the inclusion of the absorption of the negative ions of Ne, O, Na (Liu & Starace 1999; Liu 1999; Robinson & Geltman 1967; John 1975a,b; John & Williams 1975; John 1996).

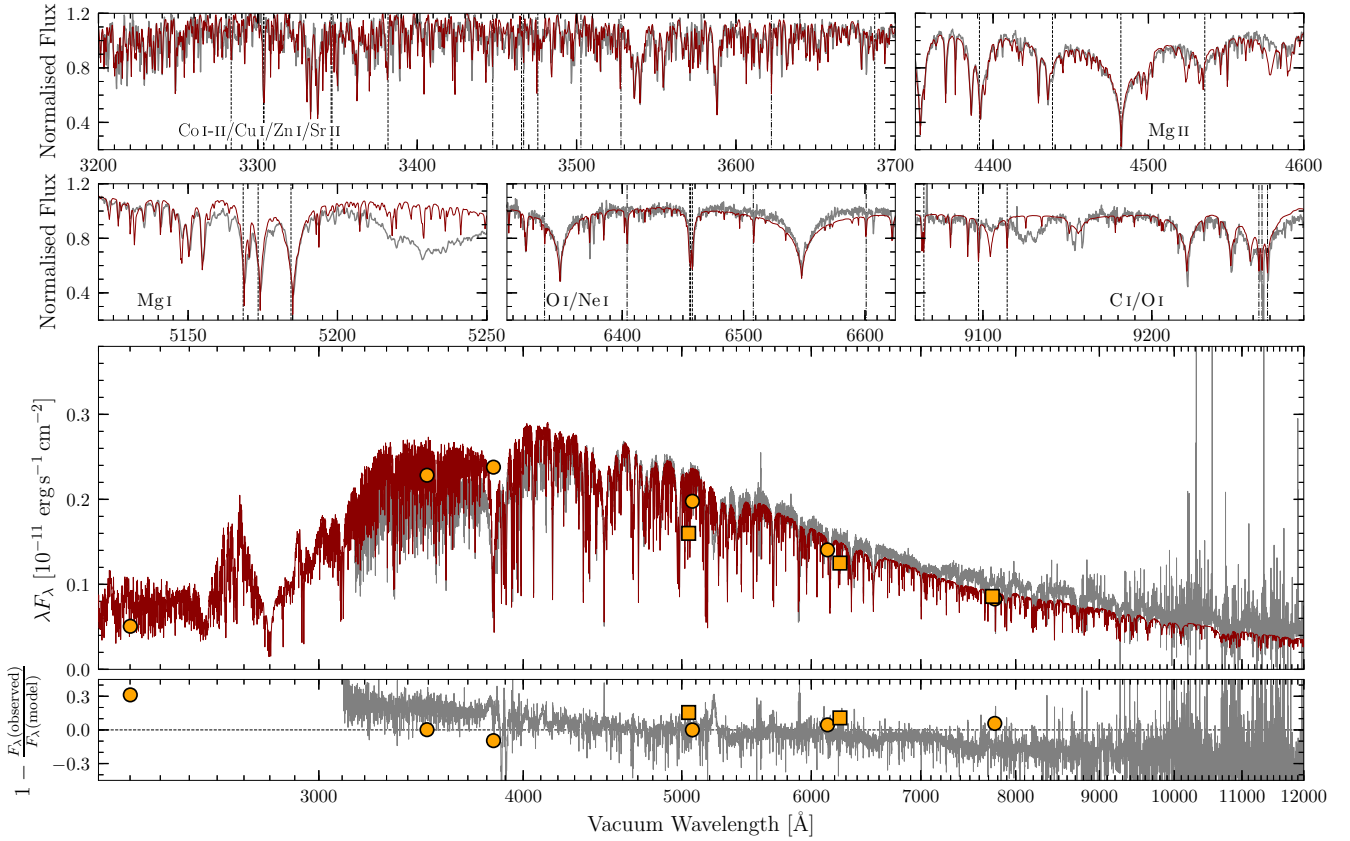


Figure 5. Comparison between the X-shooter spectrum of J1603–6613 (grey) and the best-fit synthetic spectrum (dark red). *Top panels:* The *u*-band region displaying absorption from Co, Cu, Zn, and Sr; spectral ranges containing representative examples of Mg I–II, O I, Ne I, and C I lines. *Middle panel:* De-reddened spectral energy distribution. The observed *GALEX* NUV and SkyMapper *ugri* data are over-plotted as circles, while the *Gaia* *B_p*, *G*, and *R_p* magnitudes are represented by squares (see Table 1). *Bottom panels:* Residuals between observed and synthetic spectra, and observed and synthetic photometry. The best-fit model was obtained by minimising the residuals between observed and synthetic photometry, hence the slope observed for the observed vs. synthetic spectrum comparison.

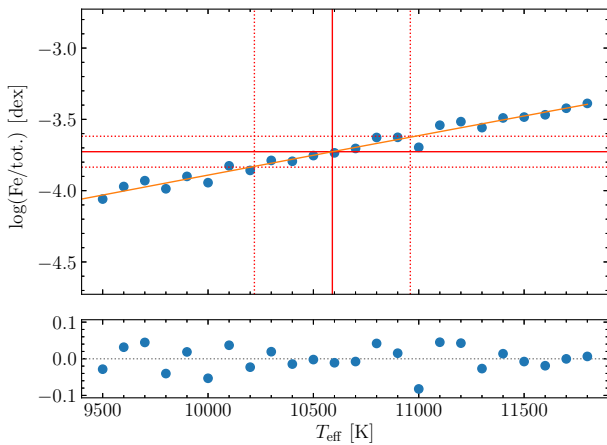


Figure 6. Estimation of the Fe abundance uncertainty for J1603–6613. The top panel shows the fit (orange) to the optimal abundance at each T_{eff} point. The bottom panel shows the residuals with standard deviation of 0.04 dex. The variation of 0.10 dex over the 370 K T_{eff} uncertainty leads to -3.73 ± 0.11 dex overall.

to be, at least, of the order of 10 Myr (this result will be relevant for the discussion in Section 5.1.2).

We initially approached the spectral analysis by fitting the X-shooter spectra alone. Given that O, Ne, and Mg, are the dominant elements and main contributors to the continuum opacity, their abundances are necessarily related to each other and coupled with T_{eff} . Hence, due to the inherent inaccuracy of flux calibration and the ill-constrained effect of interstellar reddening, the resulting atmospheric fit was strongly degenerate, in a way that adjustments in T_{eff} could be compensated for by changes in abundances, allowing for reasonable agreement with the data over a wide T_{eff} -range. We therefore tried a different approach.

Instead of allowing T_{eff} as a free parameter, we performed multiple least squares fits to the normalised spectra, but at fixed T_{eff} in steps of 100 K in the range 9500 K to 11 800 K. The optimal $\log g$ and abundances varied across the grid steps. We then used this model grid to fit SkyMapper and *GALEX* photometry (Table 1) with T_{eff} , the interstellar reddening and stellar radius as free parameters, and the *Gaia* parallax and its error used as a Gaussian prior. While *Gaia* photometry were also available, their quoted uncertainties do not include systematic errors, which are expected to be significantly larger than this. Thus, we chose

to exclude these. The best-fit was achieved by calculating synthetic photometry in each bandpass and minimising the χ^2_{ν} . This resulted in a T_{eff} of 10590 ± 370 K and a radius of $0.16 \pm 0.03 R_{\odot}$. While the full line-of-sight reddening is about $E(B - V) = 0.10$, our fit indicated a 99 per cent upper limit of 0.09 with a mean value of 0.03 in the posterior distribution, indicating the full line-of-sight extinction to be too high.

To obtain estimates for $\log g$, abundances, and their errors, we fitted the T_{eff} dependence of the element, Z , with a 2nd-order polynomial. The standard deviation of the scatter around the polynomial was taken as σ_{Z_0} , and the gradient determined at $T_{\text{eff}} = 10590$ K. Finally, the uncertainty on Z was calculated as

$$\sigma_Z^2 = \sigma_{Z_0}^2 + \left(\frac{\partial Z}{\partial T_{\text{eff}}} \right)^2 \sigma_{T_{\text{eff}}}^2, \quad (1)$$

where $\sigma_{T_{\text{eff}}} = 370$ K. We show this graphically for Fe as an example (Fig. 6). We compare the observed spectrum and our best-fit model in Fig. 5. The atmospheric parameters and the element abundances are listed in Table 4.

3.2 J1825–3757

We confirmed the radial velocity of J1825–3757, obtaining $v_{\text{rad}} = -47 \pm 3 \text{ km s}^{-1}$ from Lorentzian fits to isolated O I, Mg II, and Ca II lines of the X-shooter spectrum.

Once again we searched the spectrum to identify all elements present in the stellar atmosphere. As inferred from the bluer $B_p - R_p$ colour, J1825–3757 is hotter than both LP 40–365 and J1603–6613, and so the ionisation balance for each element is expected to be different. Apart from Cu (the higher T_{eff} does not permit detection of Cu I, and no strong optical lines of Cu II are expected), all elements found at LP 40–365 and J1603–6613 were re-identified. We note that several other elements populate higher ionisation states than found for the other two stars: Al III was identified from doublets around 3610 Å and 5710 Å, Si III from a doublet around 4560 Å, O II at 4350 Å and 4650 Å, and S II from a multitude of lines.

For the spectral analysis, we took a similar approach to that described for J1603–6613. We built a model grid between T_{eff} 11 800–14 000 K, in 100 K steps, with the surface gravity and abundances as free parameters. For the photometric fit we made use of the SkyMapper and 2MASS data (Table 1). We excluded *GALEX* photometry from our fit, because the NUV spectral region is expected to be more heavily line blanketed than found for the optical, and we cannot rule out unaccounted opacity sources, e.g. from elements presently unidentified. Using the *Gaia* parallax (Table 1) as a prior, we found $T_{\text{eff}} = 12830 \pm 450$ K, $E(B - V) = 0.080 \pm 0.017$, and $R = 0.60 \pm 0.03 R_{\odot}$.

The values and uncertainties on $\log g$ and abundances were calculated in the same manner as described for J1603–6613, and are given in Table 4. Note that, because of the higher T_{eff} , the upper-limits for hydrogen and helium are far more constraining than for LP 40–365 and J1603–6613. This strongly affirms the O Ne-dominated nature of these stars. We compare the observed spectrum and our best-fit model in Fig. 7.

A major difference in the results of J1825–3757 vs. LP 40–365 and J1603–6613 is the surface gravity, which is

more than one order of magnitude lower. This is not too surprising given the much larger radius we found for the photometric fit, implying the star is more inflated compared to the other two. This is discussed further in Section 5.1.3.

As a final comment, we examine the properties of the updated atomic data that have a more tangible effect in modelling the spectrum of J1825–3757. While our line list already included many thousands of transitions from the NIST and VALD3 databases, we noticed that the profiles of some of the weakest O I and Mg II lines were poorly reproduced by our models. In particular, three moderately strong lines at 4014, 4094, and 4110 Å (rest-frame air wavelengths) were absent in our model. From their intensities and large line widths we concluded these are most likely higher members of the Mg II series transitioning from the closely spaced 4d/f levels ($93\,311/93\,800 \text{ cm}^{-1}$, respectively), as confirmed from wavelengths tabulated by Moore (1959). We found the three missing lines (and some higher members of the series that are less obviously present) in Robert Kurucz’s line archive, which includes not only wavelengths and oscillator strengths, but also Stark, quadratic Stark, and van der Waals broadening constants. This update in our models shows a close agreement with the observed spectrum. However, we note that for the highest series members, the strengths are systematically under-predicted, likely owing to the proximity of the upper-levels to the ionisation limit, adversely affecting their estimated occupation numbers. Nevertheless, the Mg abundance was already precisely constrained by other well-known, stronger Mg II lines. The updated Mg II lines are generally weaker in the spectra of J1603–6613 and LP 40–365, because of their lower T_{eff} . Hence, their inclusion in the models leads to a minor improvement.

Although most of the strong lines are well determined in the literature, our concluding remark is that, because of their extreme photospheric composition, LP 40–365 stars necessitate complete and accurate atomic data even for lines usually considered astrophysically irrelevant.

3.3 LP 40–365

We re-analysed the prototype star, combining our new *HST*/STIS spectrum (Fig. 8) with the WHT/ISIS and Asiago 1.82-m Copernico/AFOSC spectra from Paper I. This combined, flux-calibrated spectrum has an average spectral resolution of $\approx 2\text{--}4$ Å in the optical and NUV ranges, respectively. The 5350–5700 Å region, which is only covered by the Copernico/AFOSC data, has a 13 Å resolution. We scaled the optical spectrum to the Pan-STARRS magnitude ($g = 15.635$; Flewelling et al. 2016). Although the *HST*/STIS spectrum seamlessly matches the optical fluxes, we note it is 4σ brighter than the *GALEX* NUV magnitude. The optical spectrum, instead, appears slightly bluer than the published Pan-STARRS and *Gaia* DR2 photometry, corresponding to a small colour term in the range of $B - V = -0.02$, which is comparable to the photometric uncertainties. In joining the spectra together, we transposed the optical region onto a vacuum wavelength scale to match the *HST*/STIS data (using the relation given in Morton 2000). We corrected the combined spectrum for radial velocity shift of LP 40–365 ($v_{\text{rad}} = +500 \text{ km s}^{-1}$), which is confirmed by the redshift of the C I line at 1930 Å and other strong Mg I lines. Finally, we corrected the combined spectrum for the total interstel-

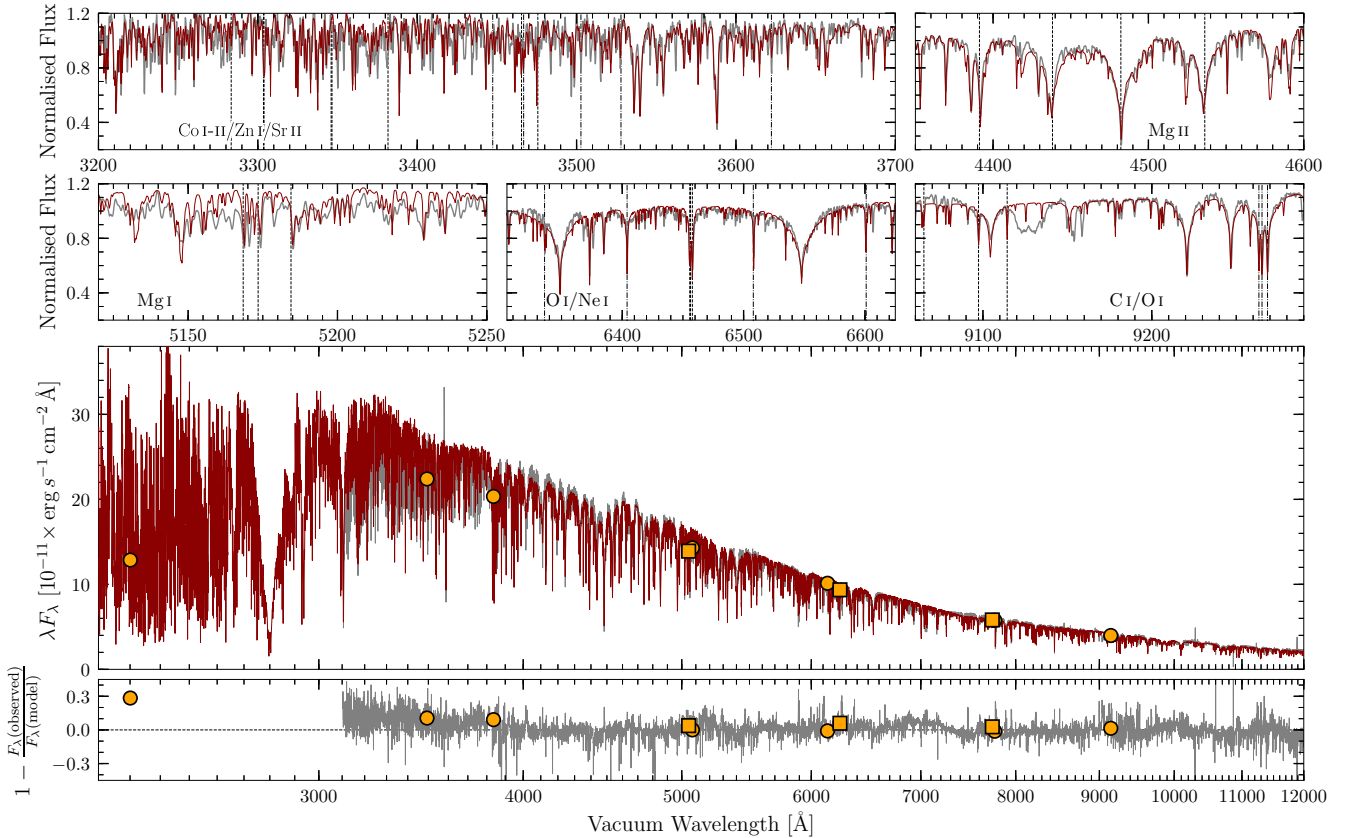


Figure 7. The X-shooter spectrum, photometry, and best-fit model for J1825–3757. Colours and symbols match those in Fig. 5.

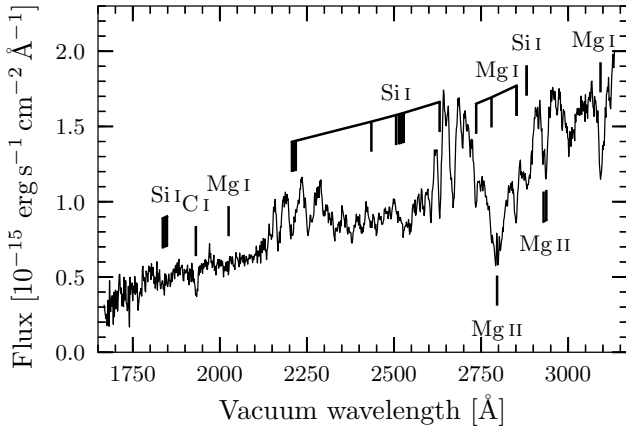


Figure 8. *HST*/STIS spectrum of LP 40–365. The red-shifted spectrum has been corrected into the laboratory rest-frame. We note the C I detection and the strongest Mg and Si lines, which cause most of the opacity in the spectrum.

lar reddening of $E(B - V) = 0.026$ (Schlegel et al. 1998), corresponding to $A_g \approx 0.09$ and $A_{\text{NUV}} \approx 0.22$ magnitudes of extinction in the Pan-STARRS g and *GALEX* NUV bands, respectively, as estimated via the Fitzpatrick (1999) standard $R_V = 3.1$ extinction law. The combined dereddened spectrum is displayed in Fig. 9.

From an initial appraisal of the combined spectrum, the

NUV data indicate a hotter temperature with respect to the optical spectrum, for which we inferred $T_{\text{eff}} = 8900$ K using a He-dominated atmosphere in Paper I. In the previous sections, we have shown the high-quality X-shooter spectra of J1603–6613 and J1825–3757 are well matched by synthetic spectra with ONe-dominated atmospheres. Especially from the analysis of J1825–3757, we have excluded the presence of He with a very stringent limit. Hence, these results favour an ONe-dominated atmosphere also for LP 40–365, as found by Vennes et al. (2017).

As we did for J1603–6613 and J1825–3757, we built a grid of synthetic models in the $T_{\text{eff}} = 8900$ –10 200 K range, with O, Ne, and Mg as dominating species. In view of the complex nature of the problem, we approached the analysis of LP 40–365 by identifying a set of key spectral features to compare against, in order to evaluate the goodness of fit and to evaluate the impact of systematic uncertainties. These are: i) the level of NUV flux; ii) the spectral lines of Ne, O, and Mg; iii) the continuum slope in the optical range; iv) the Mg I jump near 3800 Å; and v) the ionisation equilibrium of Mg I/Mg II. Because we did not find a solution that satisfies all the above criteria, we have relied more on the flux-calibrated NUV spectrum, obtaining a best-fit synthetic spectrum with $T_{\text{eff}} = 9800$ K and $\log g = 5.5$ that is shown in Fig. 9. This model approximately reproduces the NUV flux between 2200–3000 Å, the O I, Ne I, and Mg I lines, and the Mg I jump. The main defect of the synthetic spectrum is that it does not accurately reproduce the ionisation equilibrium of Mg I/Mg II, over-predicting the intensity of Mg II lines as

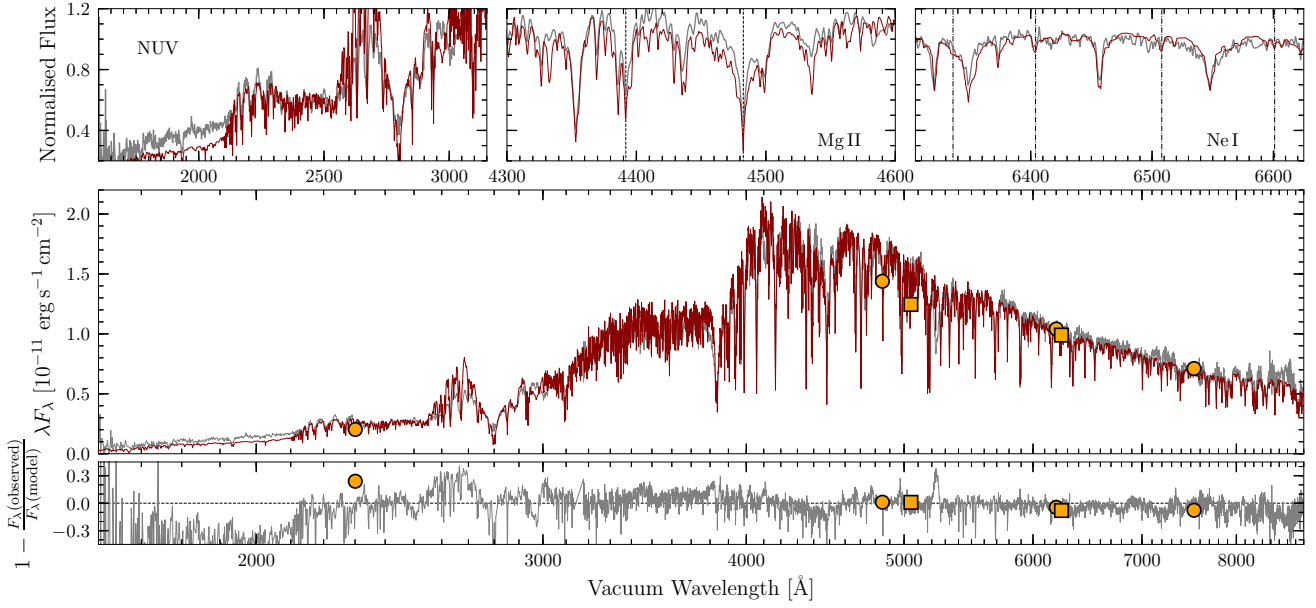


Figure 9. Comparison between the combined NUV/optical spectrum of LP 40–365 (grey) and the best-fit synthetic spectrum. Colours and symbols match those in Fig. 5 and 7. *Top panels:* Spectral ranges containing the NUV spectrum (left), the optical regions with strong Mg II transitions (centre) and Ne I lines (right), both marked by dashed vertical lines. *Middle panel:* De-reddened spectral energy distribution with the *GALEX* NUV, Pan-STARRS *gri*, and *Gaia* photometry over-plotted. *Bottom panels:* Residuals between observed and synthetic spectra, and observed and synthetic photometry.

Table 4. Composition our best-fitting synthetic spectra of LP 40–365 (Section 3.1), J1603–6613 (Section 3.2), and J1825–3757 (Section 3.3). Abundances are expressed as the number fraction of the total, $\log(Z/\text{Tot})$, where the contribution from is not included.

Parameters	LP 40–365	J1603–6613	J1825–3757
T_{eff} [K]	9800 ± 350	10590 ± 370	12830 ± 450
$\log g$ [cgs]	5.5 ± 0.3	5.34 ± 0.20	4.21 ± 0.18
v_{rad} [km s $^{-1}$]	499 ± 6	-485 ± 5	-47 ± 3
H	< -4.30	< -5.8	< -6.5
He	< -0.60	< -1.8	< -3.5
C	-2.80 ± 0.25	-3.00 ± 0.22	-3.08 ± 0.08
O	-0.46 ± 0.23	-0.45 ± 0.08	-0.44 ± 0.03
Ne	-0.27 ± 0.15	-0.22 ± 0.05	-0.21 ± 0.02
Na	-2.10 ± 0.26	-2.02 ± 0.11	-2.28 ± 0.07
Mg	-1.20 ± 0.32	-1.60 ± 0.07	-1.67 ± 0.04
Al	-2.40 ± 0.25	-2.84 ± 0.32	-3.05 ± 0.08
Si	-2.80 ± 0.25	-3.40 ± 0.17	-2.96 ± 0.05
P	< -4.30	< -5.5	< -6.4
S	-3.20 ± 0.25	-4.05 ± 0.24	-3.96 ± 0.14
Ca	-5.20 ± 0.25	-5.52 ± 0.11	-4.87 ± 0.12
Sc	< -5.40	-6.22 ± 0.26	-7.63 ± 0.35
Ti	-4.70 ± 0.34	-6.15 ± 0.19	-6.51 ± 0.11
V	< -4.40	< -7.0	< -9.2
Cr	-4.40 ± 0.35	-5.23 ± 0.22	-5.45 ± 0.09
Mn	-5.00 ± 0.35	-5.16 ± 0.18	-5.14 ± 0.05
Fe	-3.00 ± 0.25	-3.73 ± 0.11	-3.50 ± 0.03
Co	< -3.90	-4.65 ± 0.19	-4.14 ± 0.08
Ni	-3.80 ± 0.35	-4.04 ± 0.11	-4.15 ± 0.06
Cu	< -4.30	-5.50 ± 0.30	–
Zn	< -5.30	-5.20 ± 0.20	-5.50 ± 0.30
Sr	< -7.10	-8.14 ± 0.29	-8.40 ± 0.25

shown in the top-centre panel of Fig. 9. In addition, we also note that the residuals between the observed and synthetic spectra, displayed in the lower panel of Fig. 9, suggest that the optical continuum of the synthetic spectrum is slightly too steep, whereas the flux below 2200 Å is ~ 30 per cent too low. As noted in Paper I, models with increasing lower T_{eff} incur in another problem, because they have stronger Ne I lines that overpredict the observed ones.

Based on the strong coupling between O, Ne, and Mg, we estimated a 1σ T_{eff} uncertainty of 350 K, beyond which the absorption caused by these elements becomes too strong or too weak. The surface gravity cannot be constrained more precisely than $\log g = 5.5 \pm 0.3$ dex, which is compatible with a $\approx 0.16 R_{\odot}$ radius, as derived from the *Gaia* parallax and Pan-STARRS *g* magnitude, and by assuming a plausible mass between 0.15–0.60 M_{\odot} (a more detailed discussion, with reference to Paper I, is given in Section 5.1.2).

The *HST*/STIS observations have enabled a better overview of the composition of LP 40–365, clarifying the incompatibility between a He-dominated atmosphere proposed in Paper I and an ONe-dominated atmosphere, as determined by Vennes et al. (2017). This result agrees with the analysis of J1603–6613 and J1825–3757. The *HST*/STIS data favour a best-fit model with $T_{\text{eff}} = 9800$ K that is now more compatible with that determined by Vennes et al. (2017). We also note that the dominant elements of our best-fit model are in the ratio of O:Ne:Mg $\sim 34:54:6$, compared to O:Ne:Mg $\sim 50:40:2$ determined by Vennes et al. (2017).

The NUV spectrum has allowed us to detect the C I 1930 Å line, enabling us to constrain the abundance of this element. Thus, we have determined abundances for 14 elements (C, O, Ne, Na, Mg, Al, Si, S, Ca, Ti, Cr, Mn, Fe, Ni). The abundances of detected trace elements were measured by iteratively altering them, one by one, and keeping the abun-

dances of the other elements fixed. The mean values and errors are established from the means and standard deviations derived by fitting the strongest lines of each element. We have confirmed a remarkable similarity between element abundances for the three studied LP 40–365 stars (more details are given in Section 5.1.1). Finally, accounting for the coupling between T_{eff} and element abundances, we estimated the systematic uncertainties affecting our abundance determinations. On one hand, $\log(\text{O}/\text{Ne})$ slightly anti-correlates with T_{eff} , increasing by 0.05 dex for a 350 K decrease in temperature. On the other hand, $\log(\text{Mg}/\text{Ne})$ strongly correlates with T_{eff} , decreasing by 0.4 dex for a -350 K variation. All the other trace elements follow a similar trend as Mg. This result implies their mutual number abundance ratios are almost unchanged with respect to Fe, although the overall bulk atmospheric composition is affected (see Section 5.1.2).

We have also estimated upper limits on H, He, P, V, Sc, Co, Cu, Zn, and Sr. We note that Sc, Co, Zn, and Sr are detected in J1603–6613 and J1825–3757, and Cu is detected in J1603–6613. The abundances with 1σ uncertainties or upper limits are listed in Table 4.

To conclude, as discussed in the previous sections and in Paper I, it is likely that important physics may be still missing from our models. In addition to the already mentioned atomic line data, we note the lack of absorption coefficients for the bound-free and free-free contribution of Mg^+ , Al^+ , and Si^+ ions could also explain unidentified spectral features.

4 KINEMATIC ANALYSIS

Following the procedure described in Paper II for LP 40–365, we used *Gaia* DR2 astrometry and v_{rad} to trace, in a probabilistic fashion, the motion of J1603–6613 and J1825–3757 within the Milky Way potential. Using the PYTHON package for galactic dynamics, GALPY (Bovy 2015), we modelled the Milky Way’s potential with the standard module `MWPotential2014`, which includes a power-law density profile with exponential cut-off for the bulge, a Miyamoto-Nagai disc, and a dark matter halo (see details in Bovy & Rix 2013; Bovy 2015).

We imposed a Galactic disc rotation of $V_c = 239 \pm 9 \text{ km s}^{-1}$, with the Sun located at $R_0 = 8.27 \pm 0.29 \text{ kpc}$ (Schönrich 2012), accounting for a one-to-one correlation between R_0 and V_c , and a peculiar motion as determined by Schönrich et al. (2010). We sampled 10 000 boundary conditions with a Monte Carlo method, by assuming Gaussian distributions for the Galactic parameters, the radial velocities, and the astrometric parameters of the two stars. For the latter we took into account the full covariance matrix as delivered in *Gaia* DR2. The orbital parameters of J1825–3757 and J1603–6613 are summarised in Table 5, where we also list those of LP 40–365 for comparison.

Given the lack of or the low precision of *Gaia* parallaxes for the two SDSS stars, J0905+2510 and J1637+3631, we did not compute their detailed orbits. Nevertheless, we note that the radial and transverse velocities of J0905+2510, which we suggest to be another LP 40–365 star (see Section 2.5 for details), deliver a rest-frame velocity of $v_{\text{rf}} \sim 730 \text{ km s}^{-1}$, making it likely unbound from the Milky Way.

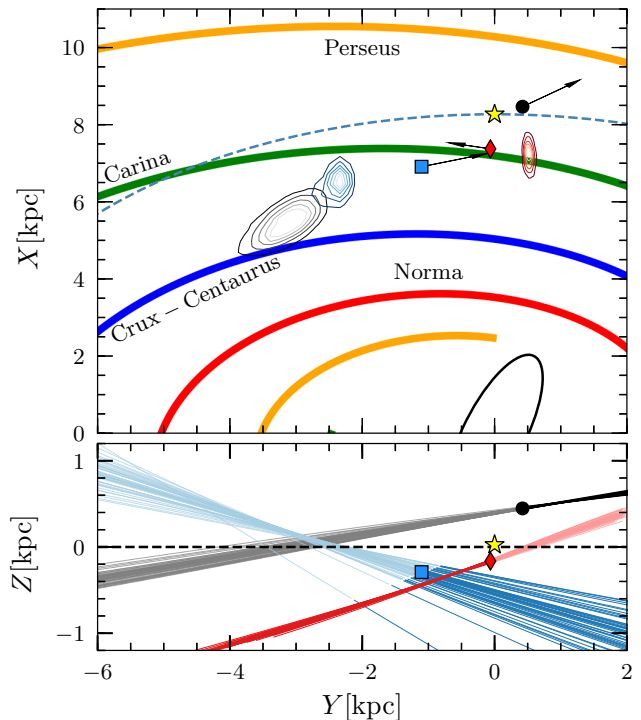


Figure 10. Sampled Galactic trajectories of LP 40–365, J1603–6613, and J1825–3757. In both panels, the Sun, LP 40–365, J1603–6613, and J1825–3757, are represented as a yellow star, black circle, blue square, and red diamond, respectively. None of the three stars crosses the Galactic plane close to its centre, excluding any ejection mechanism that requires the interaction with the super-massive black hole, Sgr A*. *Top panel:* Top-down view of the Galactic disc. The locations of spiral arms and the Galactic bar are shown as coloured and black curves (Vallée 2008). The Solar circle is traced by a dashed curve. The arrows show the mean motions of the four stars. The grey, blue, and red contours represent the Galactic disc crossing locations of LP 40–365, J1603–6613, and J1825–3757, respectively. *Bottom panel:* Representation of simulated trajectories in the Y-Z plane. The simulated trajectories are plotted as grey, blue, and red lines, for LP 40–365, J1603–6613, and J1825–3757, respectively, using lighter/darker tones for past/future positions.

4.1 The unbound trajectory of J1603–6613

Although the parallax of J1603–6613 is less precise than that of LP 40–365, we can confirm it as unbound from the Milky Way with a rest frame velocity of $v_{\text{rf}} = 805^{+49}_{-32} \text{ km s}^{-1}$, exceeding the escape velocity of $v_{\text{esc}} = 550 \text{ km s}^{-1}$ estimated with `MWPotential2014` at the corresponding Galactocentric radius of $R_G = 7 \text{ kpc}$ (cf with $\approx 520\text{--}530 \text{ km s}^{-1}$ in the Solar neighbourhood; Piffl et al. 2014; Williams et al. 2017). We show the Galactic trajectories of the three LP 40–365 stars with precise *Gaia* parallaxes in Fig. 10. J1603–6613 is escaping from the Milky Way in the southern Galactic hemisphere, while LP 40–365 is departing from the disc at positive latitudes. J1603–6613 has not yet reached its closest approach to the Sun; its spectrum is blue-shifted. Both stars move along the direction of the Galactic rotation, diverging from the tangential vectors by $\sim 20\text{--}26$ deg on average. They also have grazing trajectories with respect to the plane (≈ 5 and 10 deg for LP 40–365 and J1603–6613,

respectively), which imply a significant contribution of the Galactic rotation to the rest-frame velocity.

We note that the two unbound stars may have crossed the Galactic plane at mutually close locations, as displayed in Fig. 10, although with different flight times from the plane, $\tau_{\text{fl}} (Z = 0)$. We computed the mutual separations between the past trajectories of LP 40–365 and J1603–6613 as a function of time, finding that the minimum separation of 1 kpc might have occurred 1 Myr ago. The orbit integration confirms that their similar spectral appearance is a characteristic of the formation channel and its not related to a specific event that produced both stars at the same time.

4.2 J1825–3757 is on a Milky Way bound orbit

Combining the *Gaia* parallax and proper motions with the radial velocity of J1825–3757, we estimate a rest frame velocity of $v_{\text{rf}} = 408^{+39}_{-34} \text{ km s}^{-1}$, which is $\approx 4\sigma$ slower than $v_{\text{esc}} \approx 560 \text{ km s}^{-1}$ estimated at $R_G = 7.4 \text{ kpc}$. This implies that J1825–3757 is currently gravitationally bound to the Milky Way. For this star, we followed the orbit evolution up to 10 Gyr from now, in order to estimate the average eccentricity (e), the pericentre and apocentre, the azimuthal period, and the escape probability, which we estimate as the fraction of orbits reaching $R_G = 100 \text{ kpc}$. These and other relevant kinematic parameters are listed in Table 5.

We note that J1825–3757 is relatively close to the pericentre of the predicted orbits, and it is moving towards low Galactic coordinates, i.e. negative Z . It goes around the Milky Way once every $\approx 730 \text{ Myr}$, moving on an eccentric ($e = 0.69$), halo-like orbit against Galactic rotation. If J1825–3757 had previously crossed the Galactic plane, it would have occurred $\approx 1.5 \text{ Myr}$ ago. Its relatively large but negative vertical component of the angular momentum, $J_Z = -2800 \text{ kpc km s}^{-1}$, is consistent with its orbit being rather flat ($Z_{\text{max}} \approx 7 \text{ kpc}$). We also note that the simulated orbits reach quite large Galactic radii (apocentre at $R_G = 39^{+31}_{-14} \text{ kpc}$). A small fraction of our simulated orbits ($< 10 \text{ per cent}$) imply a possible escape of J1825–3757 from the Milky Way in the next 10 Gyr.

5 DISCUSSION

The evidence presented so far demonstrates that LP 40–365, J1603–6613, J1825–3757, and likely J0905+2510, have unique – but mutually similar – spectral characteristics and peculiar kinematics, which make them clearly distinct from other classes of stars. Our new observations strongly support the interpretation that the new stars, like LP 40–365, are the partly burnt white dwarf accretors that survived disruption from a thermonuclear supernova in a single-degenerate scenario (possibly a SNeIax, as initially advanced by Vennes et al. 2017, and further reiterated in our Paper I; Paper II). In the following sections, we will discuss the properties that identify these stars as members of what appears to be a class of “LP 40–365 stars.” We will focus on the three stars with precise *Gaia* parallaxes for which we performed a detailed spectral analysis, but our conclusions can be extended to J0905+2510, which just awaits *Gaia* to measure its parallax and proper-motions as well as a higher-quality spectrum for a detailed abundance analysis.

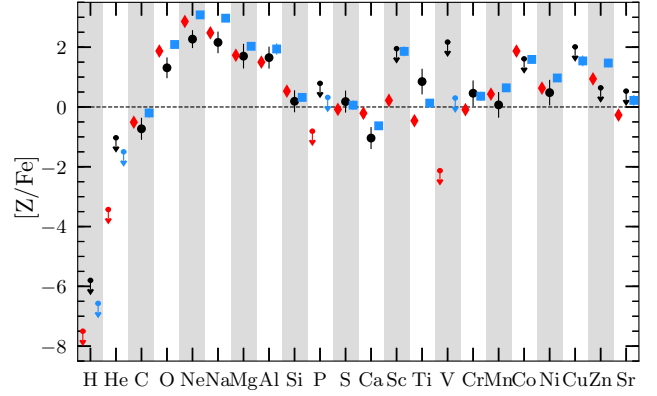


Figure 11. The elemental number abundances of LP 40–365, J1603–6613, and J1825–3757, detailed in Table 4, are displayed relatively to Fe and normalised to the Solar composition (, dashed line about 0; Asplund et al. 2009). Black circles, blue squares, and red diamonds represent LP 40–365, J1603–6613, and J1825–3757, respectively. When error bars are not visible, their size is comparable to or smaller than the symbol. Upper limits are shown as downward pointing arrows.

5.1 Physical properties

5.1.1 Atmospheric composition

The comparison among the atmospheric composition of the three LP 40–365 stars is displayed in Fig. 11, where we plot the number abundance and the upper limits of each detected element, Z , as $[Z/\text{Fe}] = \log(Z/\text{Fe}) - \log(Z/\text{Fe})_{\odot}$, where the Solar reference abundances are derived from Asplund et al. (2009).

The remarkable similarity in the average abundance pattern of LP 40–365 stars is confirmed by a typical dispersion in abundance of order 0.25 dex, which is of the order of the uncertainties, for most of the detected elements. We especially note the characteristic α enhancement and moderately super-Solar abundances of the iron-peak elements Cr, Mn, and Ni. One element that is detected in both J1603–6613 and J1825–3757, Sc, shows the largest mutual scatter ($\approx 2 \text{ dex}$). Co and Zn, also detected in J1603–6613 and J1825–3757, have the largest super-Solar abundances among the iron-group elements. Cu was marginally detected in J1603–6613, also with a super-Solar abundance. As noted in Section 3.3, the systematic uncertainties, which we estimated from the analysis of LP 40–365, affect the absolute scaling of trace metals, although they preserve the relative $[Z/\text{Fe}]$. The major effect is seen for O, Ne, and Mg, which are the bulk atmospheric constituents (see next section).

Our revised analysis of LP 40–365 with respect to Paper I now indicates an abundance, $[\text{Mn}/\text{Fe}] = 0.07$, that is closer to the Solar reference. Although the uncertainties on the abundances of LP 40–365 are relatively larger than those estimated for the other two stars (cf Section 3), it appears as the least Mn-rich of the three, with J1603–6613 and J1825–3757 having $[\text{Mn}/\text{Fe}] = 0.43$ and 0.63 dex , respectively. Given the super-Solar trend, we confirm the evidence in favour of Mn-enhancement for this group of stars. Three other elements, Cr-, Co- and Ni-to-Fe confirm a similar Super-solar trend, which strengthen the suggested connection with near- M_{Ch} thermonuclear explosions

Table 5. Orbital parameters of LP 40–365, J1603–6613, and J1825–3757.

Parameters	Symbols	LP 40–365	J1603–6613	J1825–3757
Distance [kpc]	d	0.63 ± 0.01	$1.77^{+0.40}_{-0.27}$	0.93 ± 0.05
Galactocentric radius [kpc]	R_G	$8.48^{+0.30}_{-0.28}$	$7.00^{+0.35}_{-0.38}$	$7.37^{+0.27}_{-0.31}$
Elevation [kpc]	Z	0.45 ± 0.01	$-0.29^{+0.08}_{-0.07}$	-0.16 ± 0.01
Rest frame velocity [km s^{-1}]	v_{rf}	852 ± 11	804^{+49}_{-32}	408^{+39}_{-34}
Eccentricity	e	1	1	0.69 ± 0.12
Vertical component of angular momentum [kpc km s^{-1}]	J_Z	7220 ± 250	5650 ± 310	-2800 ± 280
Maximum elevation [kpc]	Z_{max}	–	–	$7.2^{+5.8}_{-2.6}$
Pericentre [kpc]	R_{peri}	6.15 ± 0.25	6.87 ± 0.31	7.0 ± 0.30
Apocentre [kpc]	R_{apo}	–	–	39^{+31}_{-14}
Azimuthal period [Myr]	T_p	–	–	730^{+270}_{-660}
Escape probability [%]		100	100	<10
Flight time from plane crossing [Myr]	$\tau_{\text{fl}} (Z = 0)$	5.3 ± 0.5	1.66 ± 0.13	1.48 ± 0.02
Galactocentric radius at plane crossing [kpc]	$R_G (Z = 0)$	6.3 ± 0.3	6.9 ± 0.30	7.2 ± 0.3
Distance at plane crossing [kpc]	$d (Z = 0)$	$4.2^{+0.5}_{-0.2}$	$3.0^{+0.3}_{-0.2}$	$1.28^{+0.08}_{-0.07}$

(Paper I). The nucleosynthesis of these elements is known to be enhanced by electron capture that is thought to occur when the conditions for nuclear statistical equilibrium are reached at the high central densities of near- M_{Ch} explosions ($\rho > 2 \times 10^9 \text{ g cm}^{-3}$), which are expected to occur through mass-accretion from a non-degenerate companion, and not by exploding a sub- M_{Ch} white dwarf merger of $\sim 0.8 M_{\odot}$ (Iwamoto et al. 1999; Seitenzahl et al. 2013).

Super-Solar detections of Cu and Zn also agree with the observations of normal stars, for which the abundance pattern of these elements is proposed to need a significant contribution from thermonuclear supernovae that previously enriched the interstellar medium with their nucleosynthesis yields (Matteucci et al. 1993). The close-to-Solar detection of the p -nucleus, Sr, in J1603–6613 and J1825–3757 is also interesting, as this heavier element is expected to undergo significant production in the external layers of white dwarfs during thermonuclear explosions (Travaglio et al. 2011). Finally, we also note that ratios of iron-peak elements (e.g. Mn-to-Fe, Ni-to-Fe, and Mn-to-Cr mass fractions) deserve further investigation, as they could be age-estimators for the progenitors of LP 40–365 stars (e.g. via element-ratio vs metallicity relations like those employed for the characterisation of supernova nebular remnants; Badenes et al. 2008; Yamaguchi et al. 2015).

5.1.2 Comparison with theoretical yields

In Paper I, we suggested that LP 40–365 was unlikely to be the donor star in a binary supernova because its atmospheric composition, enriched with α and iron-peak elements, is incompatible with the pollution from nucleosynthesis yields of both thermonuclear and core-collapse supernovae. Considering the scenario proposed by Vennes et al. (2017), in which LP 40–365 could be the surviving white dwarf from a SN Iax explosion, in Paper I we compared its atmospheric composition to the bulk composition of theoretical “bound remnants” that form in three-dimensional hydrodynamic simulations of pure deflagrations of CO white dwarfs, which were performed by Kromer et al. (2013) and Fink et al. (2014) to reproduce the observed light curves and spectra of SNIax.

Although the abundance pattern of LP 40–365 followed the general trend of nuclear yields computed by Fink et al.

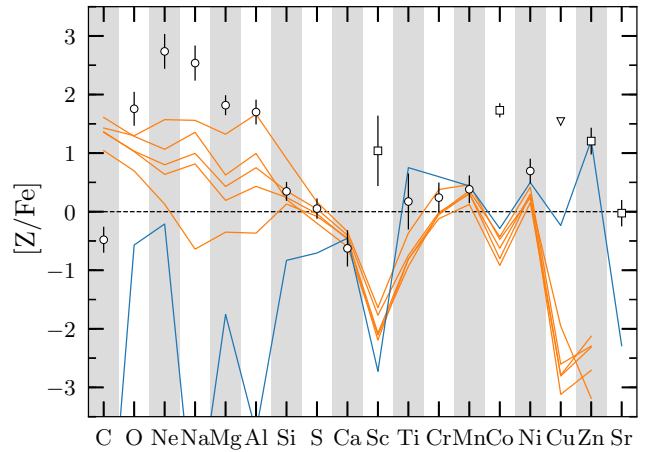


Figure 12. The average composition of LP 40–365, J1603–6613, and J1825–3757, scaled to Solar as in Fig. 11, is compared to the bulk-composition of bound remnants resulting from three-dimensional hydrodynamic simulations of pure deflagrations of CO (Fink et al. 2014) and ONe white dwarfs (Jones et al. 2019), plotted as orange and blue curves, respectively. The circles, squares, and triangle indicate whether three, two, and one star, respectively, have been used to compute the average abundances for a given element. The error bars represent the standard deviation of the variance for each element. Upper limits are not taken into account.

(2014), we noted two major conflicts with the predicted bulk-composition of bound remnants, concerning the He-dominated atmosphere and the non-detection of C (the latter was also previously noted by Vennes et al. 2017). Thanks to a more detailed analysis of LP 40–365 with the inclusion of *HST*/STIS observations and the analysis of J1825–3757 and J1603–6613 (Section 3), we have now solved the first issue by discarding the He-dominated atmosphere.

Given the similar abundance pattern of the three LP 40–365 stars, in Fig. 12, we compare their average composition to those of bound remnants computed by Fink et al. (2014). The simulations performed by these authors account for a range of internal densities of white dwarfs and explosion intensities, which lead to a wide variety of light curves and bound remnant masses (i.e. weak explosions produce

the most massive remnants and vice versa). Although the pure-deflagration models that form low-mass bound remnants were disfavoured by [Fink et al. \(2014\)](#), because their high energy output does not reproduce the observed SNIax light curves and spectra, we find them to deliver the best match to the average composition of the LP 40–365 stars (Fig. 12). The best match is obtained by a $0.1 M_{\odot}$ bound remnant, which corresponds to a progenitor with the highest central density ($5 \times 10^9 \text{ g cm}^{-3}$). However, we note that the observed abundances of the main atmospheric constituents (i.e. O, Ne, Mg) still exceed theoretical predictions by 0.5–1.5 dex. In contrast, C is at least 1.5 dex less abundant than the theoretical curves. The number abundances of trace elements, excluding Sc, Co, Cu, and Zn, are roughly within 1σ of the locus defined by bound-remnant models.

Stressing once more the remarkably similar atmospheric composition of the three LP 40–365 stars, we suggest that convection, which is predicted by our models, could play an important role. We expect the depth of convection zones of LP 40–365 stars to be physically comparable to those of a He-dominated atmospheres of similar T_{eff} , and we estimated the diffusion timescales of the detected elements to be at least ~ 10 Myr. Hence, we speculate that if SNIax bound remnant models realistically matched the abundance of Si-burning nucleosynthesis yields detected in LP 40–365 stars, either most of the left-over C might have not settled in the bound remnant or C-burning should be more intense. This interpretation requires testing via hydrodynamical calculations, which cannot currently resolve the structure of bound remnants and the expansion of supernova ejecta at the same time ([Kromer et al. 2013](#)).

An alternative scenario proposed by [Vennes et al. \(2017\)](#) might also find a compromise between low C and high O, Ne, and Mg, abundances, in case the progenitors of LP 40–365 stars were hybrid CONe white dwarfs. While the existence of hybrid CONe white dwarfs is still debated ([Denissenkov et al. 2013, 2015](#); [Brooks et al. 2017a](#)), one-dimensional computations performed by [Bravo et al. \(2016\)](#) showed that thermonuclear explosions of such stars could also form low-mass bound remnants that might represent LP 40–365 stars. However, we also note that three-dimensional hydrodynamic simulations of pure deflagrations of hybrid CONe white dwarfs suggest that bound remnants would be typically more massive ($\approx 1 M_{\odot}$; [Kromer et al. 2015](#)), in contrast with our observations (see next section).

In addition to the comparison with bound remnants from CO white dwarf explosions, we have considered the recent results obtained by [Jones et al. \(2016, 2019\)](#) for the explosion of mass-accreting ONe white dwarfs in binary systems. While these binaries are more frequently argued to form neutron stars via the accretion-induced collapse ([Schwab et al. 2015](#); [Brooks et al. 2017b](#); [Schwab & Rocha 2019](#)), three-dimensional pure-deflagration simulations performed by [Jones et al. \(2016, 2019\)](#) have shown that the nuclear burning of O and Ne could lift the electron degeneracy and explode the star, leading to what is defined as a thermonuclear electron-capture supernova (tECSN). Under these conditions, tECSNe also lead to the formation of partly burnt bound remnants, instead of neutron stars. In their work, [Jones et al. \(2019\)](#) already noted an overwhelming discrepancy with the abundance of α elements measured for LP 40–365, in contrast to a good agreement with the

iron-peak elements (Cr, Mn, Ni). Their result is confirmed via comparison with the average abundance pattern of the three LP 40–365 stars in Fig. 12. Of the new detected elements, Sc, Co, Cu, and Sr, are discrepant with respect to the tECSN model. Zn, however, displays a good match. For tECSNe to be viable progenitors of LP 40–365 stars, most of the iron-peak elements would need to be confined to the stellar interiors. This would be possible either if they were synthesised in the core of the exploded white dwarf or if they rapidly sunk after the explosion. Hence, atmospheric convection would still have a role in keeping the surface abundances as distinct as they are from the bulk composition. Furthermore, in this scenario, we note that LP 40–365 stars might eventually be the progenitors of the predicted Fe-core white dwarfs ([Isern et al. 1991](#)).

To wrap up the comparison with theoretical SNIax and tECSN bound remnants, we plotted histogram bars representing the mass fraction of detected elements (Fig. 13). The remarkable similarity among LP 40–365 stars is once again evident, with Ne as the most abundant element by mass fraction (59–65 per cent), followed by O (29–31 per cent), and Mg (3–9 per cent). The remaining elements are just 1–2 per cent of the total mass. We note that, considering the systematic uncertainties estimated from the analysis of LP 40–365, O and Ne would change by just a few per cent. However, adopting a 350 K cooler T_{eff} , the Mg mass fraction would drop to 2 per cent and all the trace elements would account for less than 1 per cent by mass. The results from theoretical simulations by [Fink et al. \(2014\)](#), instead, contain between 25–40 per cent of C and about 45 per cent of O. As noted before, the bulk compositions of theoretical bound remnants are slightly dependent on the explosion intensity and quite sensitive to central density of the accreting white dwarf. On the other hand, the bound-remnant simulated by [Jones et al. \(2019\)](#) contains 45 per cent of heavy metals, most of which are Fe and Ni.

Before concluding this section, we note that [Zhang et al. \(2019\)](#) have recently computed the evolutionary tracks and modelled the physical and spectral evolution of post-SNIax bound remnants (named postgenitors by the authors). Taking the [Kromer et al. \(2013\)](#) SNIax bound remnant composition as reference, [Zhang et al. \(2019\)](#) evolved the full stellar structure, including convection and diffusion. In contrast with our observations, their simulations, which considered a representative model of $0.6 M_{\odot}$ with an envelope accounting for 10 per cent of the mass, showed that, at late times after the bound remnants have formed ($\gtrsim 10$ Myr), the atmosphere is radiative and contains about 70, 30, and 1 per cent of C, O, and Ne, respectively, while most of the heavy elements have sunk in to the stellar interiors. The authors suggested that similar results were obtained for other lower-mass models considered.

In conclusion, the interpretation of our results, compared to theoretical work, showed that, whether LP 40–365 stars formed through either SNeIax or tECSN explosion, it would be necessary that either C-burning was more intense than what is predicted by models of CO white dwarf deflagrations or, vice-versa, less C, O, and Ne were burned in a ONe white dwarf. In both cases, we stress that theoretical results for the bulk composition of bound remnants might not reflect the atmospheric abundances, given that initial

Table 6. Physical parameters of the LP 40–365 stars. The 1σ errors and the 5–95 per cent ranges were estimated via Monte Carlo sampling. The apparent fluxes are listed without errors, because they carry very small errors from precise broad-band photometry and we did not include the effect of T_{eff} uncertainties in the error budget. The errors on radius, luminosity, and mass, account for those on parallax, T_{eff} , and $\log g$.

Parameters	Symbols	LP 40–365		J1603–6613		J1825–3757	
		16–84 %	5–95 %	16–84 %	5–95 %	16–84 %	5–95 %
Effective Temperature [K]	T_{eff}	9800 ± 300		10600 ± 370		12830 ± 450	
Surface gravity [cgs]	$\log g$	5.50 ± 0.30		5.34 ± 0.20		4.21 ± 0.18	
Luminosity [L_{\odot}]	L	0.20 ± 0.04	0.14–0.28	$0.29^{+0.13}_{-0.10}$	0.17–0.57	$8.766^{+1.82}_{-1.57}$	6.31–11.94
Radius [R_{\odot}]	R	0.16 ± 0.01	0.14–0.17	0.16 ± 0.04	0.11–0.21	0.60 ± 0.04	0.54–0.67
Mass [M_{\odot}]	M	$0.28^{+0.28}_{-0.14}$	0.09–0.87	$0.20^{+0.16}_{-0.09}$	0.07–0.51	$0.21^{+0.12}_{-0.07}$	0.10–0.44

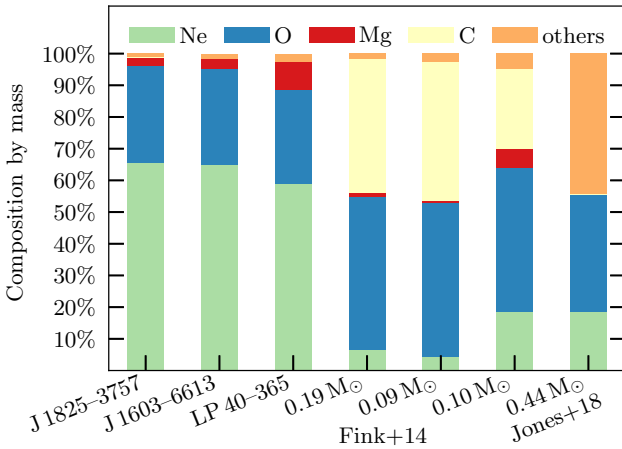


Figure 13. The atmospheres of LP 40–365 stars compared to the predicted bulk composition of three representative bound-remnants resulting from the pure deflagrations of CO white dwarfs (Fink et al. 2014) and an ONe white dwarf (Jones et al. 2019). The $0.19 M_{\odot}$ and the $0.09 M_{\odot}$ remnants result from the same initial CO white dwarf model, but the former experiences a weaker deflagration with respect to the latter. The $0.09 M_{\odot}$ and $0.10 M_{\odot}$ bound-remnants, instead, experience deflagrations of equal intensity, but the former has an initial central density that is ≈ 2 times smaller than the latter. The ONe white dwarf leading to the $0.44 M_{\odot}$ remnant has a similar structure as the CO white dwarfs, with Ne in place of C, and external stratified shells of C, He, and H.

segregation of nucleosynthetic yields, internal mixing due to gravitational settling, diffusion, and convection should definitely have a strong impact on their internal structure, atmospheric composition, and spectral evolution.

5.1.3 Masses and radii

Given the new spectral analysis of LP 40–365 presented here, we have revised our previous estimates of its physical parameters. We estimated the radius as $R = (1/\varpi)\sqrt{f/F} = 0.16 \pm 0.01 R_{\odot}$, where f and F are the extinction corrected flux and the integrated Eddington flux, respectively, both considered in the Pan-STARRS g -band. The luminosity is $L = 0.20 \pm 0.04 L_{\odot}$, as determined via the Stefan-Boltzmann law. The radius is 11 per cent smaller than what estimated in Paper II, compensating for the 10 per cent increase in T_{eff} and a more realistic spectral modelling. Considering the $\log g = 5.5 \pm 0.3$, we inferred a mass of $M = gR^2/G =$

$0.28^{+0.28}_{-0.14} M_{\odot}$ (24 per cent smaller than that of Paper II), where G is the gravitational constant.

For J1603–6613, we adopted the radius inferred from the spectro-photometric fit presented in Section 3.2, $R = 0.16 \pm 0.03 R_{\odot}$, which implies $L = 0.28^{+0.13}_{-0.10} L_{\odot}$. On the other hand, the smaller error on $\log g$ implies a more precisely constrained mass of $0.21^{+0.18}_{-0.09} M_{\odot}$.

While LP 40–365 and J1603–6613 are essentially spectroscopic twins, J1825–3757 is hotter and intrinsically brighter than the other two stars, and thus larger. The spectro-photometric fit delivered $R = 0.60 \pm 0.04 R_{\odot}$, which corresponds to $L = 8.8^{+1.8}_{-1.6} L_{\odot}$, i.e. 30 times more luminous than the two cooler stars. The inferred mass of J1825–3757, $M = 0.21^{+0.12}_{-0.07} M_{\odot}$, matches the estimates for LP 40–365 and J1603–6613.

The physical parameters of the three stars are listed in Table 6, which includes both the 1σ uncertainties and the 5–95 per cent ranges.

LP 40–365, J1603–6613, and J1825–3757 are plotted in the theoretical HR diagram (Fig. 14), where we include other classes of stars for comparison. While their T_{eff} span just ~ 2500 K, their luminosities cover two orders of magnitude (0.1 – $10 L_{\odot}$). This large portion of the HR diagram is not occupied by any long-lived phase of stellar evolution, but it is occasionally scattered with (pre-) low-mass He-core white dwarfs, which are the products of binary interaction (Istrate et al. 2016), metal-poor A/F-type stars (Pelisoli et al. 2019), and short-lived evolutionary phases with stochastic behaviour, like cataclysmic variables or millisecond pulsar companions. J1603–6613 sits very close to LP 40–365, as expected for two spectroscopically and photometrically similar stars. Although J1825–3757 appears closer to the zero-age extreme horizontal branch and the main sequence (note the log-log scale), it is ~ 15000 K cooler but larger than equal-luminosity hot subdwarfs. Hence, it is at least an order of magnitude less luminous than equal- T_{eff} main sequence stars.

Given their unusual, “sub-luminous” location in the HR diagram and their small masses, which are below the typical mass of canonical white dwarfs (e.g. $0.621 M_{\odot}$; Tremblay et al. 2016), we speculated that the interiors of LP 40–365 stars may not be fully degenerate. We measured their average densities as $\bar{\rho} \approx 340, 240$, and 4.5 g cm^{-3} for LP 40–365, J1603–6613, and J1825–3757, respectively. Hence, we note that LP 40–365 and J1603–6613 have average densities that are comparable to those of brown dwarfs (or hot subdwarfs), whereas the mean density of J1825–3757 is similar to that of the Sun.

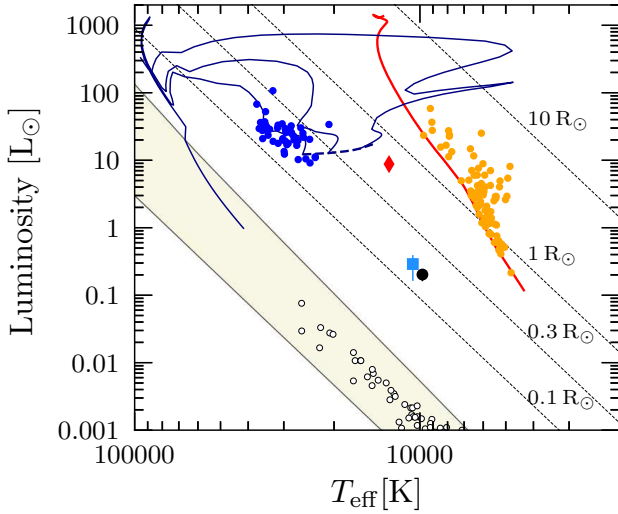


Figure 14. Theoretical HR diagram displaying LP 40–365 (black circle), J1603–6613 (light-blue square), and J1825–3757 (red diamond), along with representative samples of hot subdwarfs (blue circles; Lisker et al. 2005), main-sequence stars (orange circles; Boyajian et al. 2013), and white dwarfs in the Solar neighbourhood (white circles; Giammichele et al. 2012). We note that the 1σ errors on the estimated physical parameters are smaller or of the order of the symbol sizes (on the adopted log-log scale). For reference, we draw the canonical-mass white dwarf cooling sequence (beige-coloured strip Fontaine et al. 2001), the 100 Myr old main-sequence (red curve; Choi et al. 2016), and the evolutionary tracks for 0.47, 0.48, and 0.50 M_{\odot} hot subdwarfs (blue curves; Dorman et al. 1993). The luminosities for given stellar radii are shown as a function of T_{eff} (dotted curves).

Finally, as discussed in Paper I, we remark that the radii we measure for LP 40–365 stars are in agreement with the observed low-rotation rates. We note that, even if their progenitors were tidally locked in a short period binary (see Section 5.1.5 and Fuller & Lai 2012), we expect that mass loss and radius expansion caused by the supernova explosion could have both contributed to slow down a potentially fast-rotating star.

5.1.4 Evolutionary timescales

Given their rarity, the current location of the LP 40–365 stars in the HR diagram of Fig. 14 is likely transitory and it is probably characterised by a relatively fast evolution, which could be shorter than the Galactic crossing time for the unbound stars (~ 140 Myr for LP 40–365; Paper II).

Shen & Schwab (2017) modelled the first ~ 1000 yr of evolution for post-SNeIax bound remnants. In this early phase, the stellar photosphere is initially inflated to $> 1000 R_{\odot}$, the energy output is dominated by strong winds that are powered by the decay of radioactive ^{56}Ni and ^{56}Co , and the release of energy takes place over ~ 10 – 100 yr timescales. More recent work by Zhang et al. (2019) covers the long-term evolution of post-SN Iax bound remnants, specifically discussing LP 40–365 as one such star. These authors proposed that post-SN Iax bound remnants would initially cool down over relatively short time scales, and then heat up and brighten during an at-least 10 Myr-long

timescale until they reach the white dwarf cooling sequence again. This mechanism would be regulated by convection and diffusion of iron-peak elements, which initially would settle in the atmosphere of the bound remnants for 10,000 yr during the early phase and would cause a large opacity. The long-lived brightening phase would be caused by a sharp decrease of iron-peak element abundances when the bound remnant becomes radiative and warms up again, after reaching its minimum luminosity and coolest temperature that depend on its mass and envelope size.

Despite finding a poor agreement with the atmospheric composition of LP 40–365, Zhang et al. (2019) identified a good match between its location in the HR diagram and the evolutionary track computed for a 0.15 M_{\odot} post-SN Iax bound remnant. This result is intriguingly close to the updated masses of LP 40–365 and J1603–6613. Thus, Zhang et al. (2019) estimated for LP 40–365 an age of 23 Myr, which corresponds to the peak of brightness of the long-lived phase. While J1603–6613 would have a similar age as LP 40–365, it would seem that J1825–3757 is older than the other two stars by interpolating between the Zhang et al. (2019) tracks for 0.15–0.3 M_{\odot} remnants. Hence, this star might be about to join the white dwarf cooling track over a relatively sort time.

The presence of iron-peak elements in the atmosphere of LP 40–365 stars critically contrasts with the models of Zhang et al. (2019) and it could indicate that the decline of stellar luminosity is characterised by much longer timescales. Hence, the relative ages of the three LP 40–365 stars could be inverted, i.e. J1825–3757 and would be the youngest of the three objects. For quantifying this, we estimated the Kelvin-Helmholtz timescales, τ_{KH} , for the three LP 40–365 stars that, in absence of internal sources of energy production, is a good estimator for the evolutionary timescales. Adopting the formulation $\tau_{\text{KH}} = 3GM^2/7RL$, which holds for a wide range of objects with internal structure reproducible by a polytrope with index $n = 3/2$, and using the values from Table 6, we obtain $\tau_{\text{KH}} \sim 32, 12, 0.1$ Myr for LP 40–365, J1603–6613, and J1825–3757, respectively. The τ_{KH} of LP 40–365 and J1603–6613 are broadly compatible the evolutionary age estimated by Zhang et al. (2019). The τ_{KH} of J1825–3757 suggests a much younger age that is, however, larger than the rapid cooling phase of the Zhang et al. (2019) models that is richer in atmospheric iron-peak elements (100–10,000 yr). We note that such a short τ_{KH} is still compatible with the non-association of J1825–3757 with known diffuse nebulae caused by young supernova.

5.1.5 Kinematics and birth places

The rest frame velocities of LP 40–365 and J1603–6613 ($v_{\text{rf}} \approx 800$ – 850 km s^{-1}) are compatible with the two stars being unbound from the Milky Way. This condition implies that, in absence of a powerful birth kick, both stars took advantage of a large boost from the Milky Way rotation so that $v_{\text{rf}}^2 = V_{\text{c}}^2 + v_{\text{ej}}^2 + 2V_{\text{c}} v_{\text{ej}} \cos \alpha \cos \beta = 800$ – 850 km s^{-1} , where α and β are the angles drawn by the ejection velocity vector, v_{ej} , with respect to the vertical direction and the Galactic rotation, respectively. Considering the almost-parallel alignment of the trajectories of LP 40–365 and J1603–6613 in the $X - Y$ plane (5 – 10 deg with respect to direction of the

Galactic rotation in the plane, and 20–26 deg with respect to the vertical direction), we found the minimum possible ejection velocities in the range of $v_{\text{ej}} \approx 550\text{--}600 \text{ km s}^{-1}$.

In order to achieve the smallest v_{ej} possible, obtainable with the maximum benefit from V_c , the supernovae should have exploded at relatively close distances from the Galactic plane and not too far away from the centre (we note that V_c is already ~ 10 per cent slower above $|Z| = 1 \text{ kpc}$, and it stays constant up to $R_G \approx 25 \text{ kpc}$; Williams et al. 2013; Huang et al. 2016). This condition is compatible with the prediction for runaway stars ejected by a disc-like distribution of supernova progenitors (Kenyon et al. 2014).

Adopting the Zhang et al. (2019) age estimate of 23 Myr as the flight time for both LP 40–365 and J1603–6613, we could track their simulated trajectories back to the fourth and third Galactic quadrants, respectively. We note that the $R_G \sim 25 \text{ kpc}$ estimated by Zhang et al. (2019) does not account for the past trajectory of LP 40–365, and it is rather equivalent to the radial distance that would be covered in 23 Myr at 850 km s^{-1} . Hence, properly tracing the Galactic orbits, we find that LP 40–365 and J1603–6613 would have been ejected from possible birth sites at $R_G \approx 15 \text{ kpc}$ and $Z \approx -1.2 \text{ kpc}$, and $R_G \approx 17 \text{ kpc}$ and $Z \approx +3.4 \text{ kpc}$, respectively. These coordinates are roughly compatible with birth sites within the thick disc. Furthermore, we note the Galactocentric radii of the identified birth sites are close to the empirical determination for the edge of the Galactic disc, i.e. where most of the star formation is seen to take place (within a $R_G = 13\text{--}16 \text{ kpc}$ cut-off, as observed from photometric surveys of the Milky Way Sale et al. 2010; Minniti et al. 2011). Thus, this result agrees with SN Iax observations, which are mostly seen in association with regions of recent or ongoing star formation (Foley et al. 2013; Jha 2017; Lyman et al. 2018). On the other hand, if we wanted to impose birth sites that are nearer to the plane, say $|Z| = 1$, to find a better match with the minimum $v_{\text{ej}} = 600 \text{ km s}^{-1}$, we would obtain $R_G = 12, 8 \text{ kpc}$ and $\tau_{\text{fl}} = 19, 7.5 \text{ Myr}$ for LP 40–365 and J1603–6613, respectively.

We previously noted that J1825–3757 is bound to the Milky Way. The fact that it moves in the opposite direction with respect to the Galactic rotation and it follows a fairly eccentric orbit strongly supports the supernova-ejection mechanism. Observing that the direction of motion of this star has an equally small inclination with respect to the Galactic plane (a few degrees) as the other two, and it is a ~ 165 deg with respect to the Galactic rotation, we also estimated a minimum ejection velocity of $v_{\text{ej}} \approx 600 \text{ km s}^{-1}$. Finally, we note that if J1825–3757 is as young as $\tau_{\text{KH}} \sim 0.1 \text{ Myr}$, it would have formed within the thin disc.

5.1.6 Binary progenitors

Given that we find similar v_{ej} for the three LP 40–365 stars, it is reasonable to think they formed from the disruption of similar binary progenitors. In the ideal case of instantaneous mass loss and no interactions between accretor and donor stars (Hills 1983), $v_{\text{ej}} \sim 550\text{--}600 \text{ km s}^{-1}$ are lower limits on the orbital velocity at the moment of explosion. This condition could be met if the progenitors of LP 40–365 stars were white dwarfs of $M \geq 1.2 M_\odot$, which were orbited by $0.8\text{--}1.3 M_\odot$ He-burning donor stars in $\approx 1 \text{ hr}$ (Paper II). This re-

sult is compatible with a single-degenerate scenario proposed for SN Iax (including progenitors with CO and hybrid CONE cores; Wang & Han 2009; Wang et al. 2013, 2014), and may also be representative of accreting ONe white dwarfs that lead to tECSNe. We note that kicks due to asymmetric explosions and interactions with the both the donor star and supernova ejecta are expected to take place (Marietta et al. 2000; Jordan et al. 2012; Pan et al. 2012; Liu et al. 2013), adding complexity to this interpretation.

The rest frame velocities of the unbound LP 40–365 stars contrasts with the much larger $v_{\text{rf}} \gtrsim 1000 \text{ km s}^{-1}$ of the other known hyper-runaway stars, i.e. the D^6 stars (proposed as the former donor white dwarfs in double-degenerate supernova progenitors; Shen et al. 2018b) and the hot subdwarf star US 708 (proposed to be the former low-mass He subdwarf donor in a single-degenerate sub- M_{Ch} supernova; Geier et al. 2015). Hence, the kinematics of LP 40–365 stars confirms their origin from a distinct class of binary progenitors, also exploding as thermonuclear supernovae, but possessing smaller orbital velocities than the D^6 and US 708 progenitors.

5.2 Prospects for end-of-mission *Gaia* detections

Zhang et al. (2019) have estimated that four post-SN Iax stars would be detectable within 2 kpc from the Sun. In contrast, Shen et al. (2018b) estimated the number of D^6 stars in *Gaia* as 14–40 within 1 kpc. The results obtained by these authors are comparable, considering that empirical SN Iax rates are typically estimated to occur as 1–30 per cent of the SN Ia rates (Foley et al. 2013; Li et al. 2011a; Graur et al. 2017; Jha 2017). Although Zhang et al. (2019) considered LP 40–365 stars as good candidates for the post-SN Iax bound remnants, they assumed these runaways to have $v_{\text{rf}} \sim 1000 \text{ km s}^{-1}$. Such large velocities have only been measured for D^6 stars and the hot subdwarf US 708. Given the smaller v_{rf} of LP 40–365 stars, likely due to their different binary progenitors, we re-estimated their space density.

Assuming the progenitors of LP 40–365 stars have a space density reflecting that of the Galactic thin disc, we distributed them according to an exponentially decaying profile (scale-height and scale-length of 0.3 and 3 kpc, respectively). We scaled the formation rate of LP 40–365 stars to 10 per cent of the Galactic SN Ia rate of $10^{-13} \text{ yr}^{-1} M_\odot^{-1}$ (Li et al. 2011b), as adopted by Shen et al. (2018b). This rate is compatible with the average of other estimates from the literature, which include a mix of progenitors from both the single- and double-degenerate channels (i.e. SNe Ia with a variety of delay times; Scannapieco & Bildsten 2005; Mannucci et al. 2005, 2006; Aubourg et al. 2008; Ruiter et al. 2009; Maoz et al. 2011). Hence, considering a Galactic disc mass of $\approx 5 \times 10^{10} M_\odot$ (Bland-Hawthorn & Gerhard 2016), we created 50,000 objects with birth-times that were uniformly distributed over a time interval of 100 Myr, $t_0 = \mathcal{U}(0, 100)$. We assigned Gaussian-distributed initial velocities, $v_{\text{ej}} = \mathcal{N}(600, 25)$, which we modelled on those we have inferred for the observed LP 40–365. Finally, we used GALPY to estimate the kinematic parameters after a flight time of $\tau_{\text{fl}} = (100 - t_0) \text{ Myr}$.

Running ten simulations to randomise the initial condi-

tions, we counted 78 ± 8 objects within 2 kpc. Such an estimate included all objects with a $\tau_{\text{H}} \leq 100$ Myr. However, we know that a large fraction of them might not be detectable for several reasons, one of which is the long-term evolution of their absolute magnitudes. If we considered that LP 40–365 stars evolve as proposed by Zhang et al. (2019), i.e. they are 10–1000 times fainter than LP 40–365 in their first ~ 10 Myr of life, we would expect that only those older than 20 Myr (i.e. 63 ± 6) are detectable by *Gaia* with $G < 18$ (assuming the absolute magnitude of LP 40–365, $M_G = 6.5$, as a lower limit). Hence, we could expect to detect just 1–3 intrinsically fainter, younger LP 40–365 stars in a smaller volume (e.g. $d < 1$ kpc) down to $G = 19$.

The estimate of 63 stars might be optimistic, given that so far we have detected just three LP 40–365 stars within 2 kpc, suggesting that the timescales proposed by Zhang et al. (2019) are too short. Following this interpretation, all the observed LP 40–365 stars are still relatively young, having ages of the same order of magnitude or shorter than the $\tau_{\text{KH}} \sim 32$ Myr measured for LP 40–365. In this case, we would expect 22 ± 4 LP 40–365 stars. Although this estimate is still too large in comparison with the observed numbers, we note a better agreement with the predictions by Shen et al. (2018b), if we scale our estimate to the number of D⁶ stars within a smaller volume with a 1 kpc radius.

Given their relatively low v_{ej} , most of the LP 40–365 stars could stay bound to the Milky Way, as we find that just ≈ 20 per cent of the simulated objects have $v_{\text{rf}} > v_{\text{esc}}$. The fraction of stars achieving $v_{\text{rf}} > 1.3 v_{\text{esc}}$ is just 4 per cent of the total. Typical proper motions of LP 40–365 stars would also be relatively small, with an average value of $\mu = 49^{+33}_{-20}$ mas, indicating that LP 40–365 and J1825–3757 could be the rarest outliers in the μ distribution.

While we stress that these simulations are affected by several unknowns such as the confirmation of a cooling law and the variety of supernova rates, we note that they are sufficiently straightforward to motivate further spectroscopic follow-up of LP 40–365 star candidates. We also note that the binary-supernova mechanism implies the existence of ejected donor stars, which may have similar kinematics, but different compositions.

Finally, we note that the results of this section can also be extended to the ONe white dwarfs that may explode as tECSNe, for which Jones et al. (2019) estimated a birth rate of $\sim 10^{-14} \text{ yr}^{-1} M_{\odot}^{-1}$, which is of the same order of magnitude of that adopted for SN-Iax bound remnants. Thus, tECSNe might lead to the formation of ~ 20 detectable LP 40–365 stars within 2 kpc from the Sun.

6 SUMMARY AND CONCLUSIONS

Through detailed spectroscopic, photometric, and kinematic analysis, we have gained further evidence in favour of the idea initially advanced by Vennes et al. (2017) and then reinforced in Paper I and Paper II that the high-velocity star LP 40–365 could be a partly burnt white dwarf accretor that survived to a peculiar class of thermonuclear supernovae occurring in binary systems. Given the striking spectroscopic and kinematic similarity we found among LP 40–365 and three new objects (J1603–6613, J1825–3757, J0905+2510), we propose this star as the namesake of its own spectral

class that is defined both by spectroscopic, physical, and kinematic properties:

- (i) Ne-dominated atmospheres, with O and Mg as the second- and third-most-abundant elements, respectively.
- (ii) Broadly homogeneous composition of detected trace elements (C, Na, Al, Si, S, Ca, Sc, Ti, Cr, Mn, Fe, Co, Ni, Cu, Zn, Sr).
- (iii) Low mass, below the canonical white dwarf mass.
- (iv) Ejection velocity in the range of 550–600 km s^{−1}.

The atmospheric composition of LP 40–365 stars is a strong indication of partial C-, O-, and Si-burning, likely connected to thermonuclear explosions that did not entirely disrupt their progenitors. Of significant note is the near-identical spectroscopic properties of both LP 40–365 and J1603–6613, which strongly suggests a similar formation mechanism. We found some similarities with the simulations of pure deflagrations of CO and ONe white dwarfs, which could be representative of SNeIax (Fink et al. 2014) and thermonuclear electron-capture supernovae (Jones et al. 2019), respectively. We noted that the models do not reproduce the main atmospheric components (O, Ne, Mg), perhaps because the bulk composition of bound remnants is not represented by the photosphere of these stars. Promising simulations by Zhang et al. (2019) describe, for the first time, the evolution of post-SN Iax stars. However, the temporal evolution does not well match those of the LP 40–365 stars. New theoretical evolutionary models are required, which better account for the initial stratification of nucleosynthetic yields within bound remnants, internal mixing, convection, and diffusion, and also including the evolution of hybrid CONe white dwarfs.

The physical properties of LP 40–365 stars are precisely constrained by our spectral analysis and *Gaia* parallaxes, indicating a relatively small range of masses (median masses between 0.20–0.28 M_{\odot}), which indicates they currently are (not fully degenerate) low-mass objects. The radii of these stars were likely inflated due to the large energy accumulated during and after the supernova explosion, growing to 0.16–0.60 R_{\odot} , roughly an order of magnitude larger than typical white dwarf radii. Such a large range is compatible with the stars being caught at different evolutionary stages. While the Zhang et al. (2019) models predicted the LP 40–365 stars could be older than ~ 23 Myr, we speculated that LP 40–365 stars could be still relatively unevolved and thus younger than the Kelvin-Helmholtz timescale of LP 40–365 (~ 32 Myr), due to the large abundance of heavy metals in their atmospheres.

The kinematics of LP 40–365 stars are also distinctive, indicative of their formation mechanism. We found that they can be either bound or unbound to the Milky Way, depending on whether the stars were ejected in the direction of Galactic rotation (as with LP 40–365 and J1603–6613) or in the opposite direction (like J1825–3757). In order to obtain the observed kinematics, confined to small Z coordinates, the progenitors of LP 40–365 stars likely resided in the Galactic disc, further constraining their ages to no more than a few 10 Myr. The ejection velocities required to reproduce the rest-frame velocity of the three LP 40–365 stars are in the range of 550–600 km s^{−1}, consistent with ejection from a relatively compact binary systems containing a the near- M_{Ch} white dwarf progenitor and a He-burning donor

star of roughly $0.8\text{--}1.3\text{ M}_{\odot}$ orbiting with a ~ 1 hr period. This result is at least compatible with one class of thermonuclear supernova progenitors, which are invoked to explain short-delay-time supernovae and subluminal classes like SNe Iax (Wang & Han 2009; Wang et al. 2009a,b, 2013). Furthermore, we noted that the kinematic evidence characterising LP 40–365 stars clearly distinguishes them from other groups of hyper-runaways, i.e. the D^6 stars (Shen et al. 2018b) and the hot-subdwarf US 708 (Geier et al. 2015), which require even more compact progenitors to reach their rest frame velocities of $\gtrsim 1000\text{ km s}^{-1}$.

We estimate that of the order 22 stars could be detectable by the end of the *Gaia* mission if LP 40–365 stars are post-SN Iax stars, imposing the boundary conditions implied by the ejection velocities and flight times determined from our analysis. Although the results of our simulations were susceptible to large variations, e.g. the uncertainty of supernova rates and evolutionary timescales of LP 40–365 stars, we stress they are compatible with the observed numbers and scale as 10 per cent of predicted D^6 stars (Shen et al. 2018b). We also noted that the results of our predictions for future *Gaia* detection are compatible with the possibility that LP 40–365 stars could be bound remnants surviving to tECSNe.

The key message from our simulation of the population of LP 40–365 stars within 2 kpc of the Sun is that most of them are likely gravitationally bound to the Milky Way and will possess relatively small proper motions. The confirmed LP 40–365 stars may not represent the broader population yet to be discovered, suggesting that evolutionary “missing links” as well as their ejected donor stars are yet to be found. It is possible that more evolved LP 40–365 stars would show different atmospheric compositions, if their heavy elements sink deeper into the atmosphere as the stars evolve with changing temperatures and radii. We anticipate interesting results from more advanced theoretical modelling, expanding the results presented by Fink et al. (2014), Kromer et al. (2015), and Jones et al. (2019) for the composition of bound remnants and Zhang et al. (2019) for the late cooling of SN Iax bound remnants.

Finally, we remark that the LP 40–365 stars that remain bound to the Milky Way could revert back to the white dwarf cooling sequence, likely within a few 100 Myr, still displaying lower $\log g$ than canonical white dwarfs due to their smaller masses. These white dwarfs should have stratified atmospheres, containing mostly O, Ne, and Mg. Although not fully investigated, peculiar O-rich white dwarfs like J1240+6710 (Kepler et al. 2016) – as well as one of our SDSS candidates, J1637+3631 – could represent or be linked to one of the final evolutionary stages of the newly discovered class of LP 40–365 stars.

ACKNOWLEDGEMENTS

We thank S. O. Kepler, R. Fisher, A. Rebassa-Mansergas, S. Toonen, M. Zhang, and C. Wheeler for their helpful feedback during EUROWD21 at the University of Texas at Austin, A. Irrgang for discussions on Galactic trajectories, and S. Jones for kindly providing his bound remnant compositions in machine-readable format.

RR and UH acknowledge funding by the German Sci-

ence foundation (DFG) through grants HE1356/71-1 and IR190/1-1. Support for JJH was provided by NASA through Hubble Fellowship grant #HST-HF2-51357.001-A, awarded by the Space Telescope Science Institute, which is operated by the Association of Universities for Research in Astronomy, Incorporated, under NASA contract NAS5-26555. IP acknowledges support from DFG under grant GE 2056-12-1. JS acknowledges support from the Packard Foundation. The research leading to these results has received funding from the European Research Council under the European Union’s Horizon 2020 research and innovation programme no. 677706 (WD3D) and the European Union’s Seventh Framework Programme (FP/2007-2013) / ERC Grant Agreement no. 320964 (WDTracer). OFT and BTG were supported by the UK STFC grant ST/P000495.

This work has made use of data from the European Space Agency (ESA) mission *Gaia* (<https://www.cosmos.esa.int/gaia>), processed by the *Gaia* Data Processing and Analysis Consortium (DPAC, <https://www.cosmos.esa.int/web/gaia/dpac/consortium>). Funding for the DPAC has been provided by national institutions, in particular the institutions participating in the *Gaia* Multilateral Agreement. Based on observations made with the NASA/ESA HST, obtained at the Space Telescope Science Institute, which is operated by the Association of Universities for Research in Astronomy, Inc., under NASA contract NAS 5-26555. These observations are associated with program 15431. Based on observations made with ESO Telescopes at the La Silla Paranal Observatory under programme ID 093.D-0431, 097.D-1029, and 0101.C-0646. Based on observations obtained at the Southern Astrophysical Research (SOAR) telescope, which is a joint project of the Ministério da Ciência, Tecnologia, Inovações e Comunicações (MCTIC) do Brasil, the U.S. National Optical Astronomy Observatory (NOAO), the University of North Carolina at Chapel Hill (UNC), and Michigan State University (MSU). Also based on observations collected at Copernico telescope (Asiago, Italy) of the INAF – Osservatorio Astronomico di Padova. The William Herschel Telescope and its service programme are operated on the island of La Palma by the Isaac Newton Group of Telescopes in the Spanish Observatorio del Roque de los Muchachos of the Instituto de Astrofísica de Canarias (prog. ID: W/2017A/25, W/2017A/30, and SW2017a12).

Funding for the Sloan Digital Sky Survey IV has been provided by the Alfred P. Sloan Foundation, the U.S. Department of Energy Office of Science, and the Participating Institutions. SDSS-IV acknowledges support and resources from the Center for High-Performance Computing at the University of Utah. The SDSS web site is www.sdss.org.

This research made use of Astropy, a community-developed core Python package for Astronomy (Astropy Collaboration et al. 2018).

REFERENCES

- Abolfathi B., et al., 2018, *ApJS*, **235**, 42
- Asplund M., Grevesse N., Sauval A. J., Scott P., 2009, *ARA&A*, **47**, 481
- Astropy Collaboration et al., 2018, *AJ*, **156**, 123
- Aubourg É., Tojeiro R., Jimenez R., Heavens A., Strauss M. A., Spergel D. N., 2008, *A&A*, **492**, 631

- Badenes C., Bravo E., Hughes J. P., 2008, *ApJ*, **680**, L33
- Bailer-Jones C. A. L., Rybizki J., Fouesneau M., Mantelet G., Andrae R., 2018, *AJ*, **156**, 58
- Bergeron P., Leggett S. K., Ruiz M. T., 2001, *ApJS*, **133**, 413
- Bland-Hawthorn J., Gerhard O., 2016, *ARA&A*, **54**, 529
- Bovy J., 2015, *ApJS*, **216**, 29
- Bovy J., Rix H.-W., 2013, *ApJ*, **779**, 115
- Boyajian T. S., et al., 2013, *ApJ*, **771**, 40
- Bravo E., Gil-Pons P., Gutiérrez J. L., Doherty C. L., 2016, *A&A*, **589**, A38
- Brooks J., Schwab J., Bildsten L., Quataert E., Paxton B., 2017a, *ApJ*, **834**, L9
- Brooks J., Schwab J., Bildsten L., Quataert E., Paxton B., 2017b, *ApJ*, **843**, 151
- Buzzoni B., et al., 1984, *The Messenger*, **38**, 9
- Chambers K. C., et al., 2016, preprint, [p. arXiv:1612.05560](https://arxiv.org/abs/1612.05560) ([arXiv:1612.05560](https://arxiv.org/abs/1612.05560))
- Choi J., Dotter A., Conroy C., Cantiello M., Paxton B., Johnson B. D., 2016, *ApJ*, **823**, 102
- Clemens J. C., Crain J. A., Anderson R., 2004, in Moorwood A. F. M., Iye M., eds, *Proc. SPIE Vol. 5492, Ground-based Instrumentation for Astronomy*. pp 331–340, [doi:10.1117/12.550069](https://doi.org/10.1117/12.550069)
- Currie M. J., Berry D. S., Jenness T., Gibb A. G., Bell G. S., Draper P. W., 2014, in Manset N., Forshay P., eds, *Astronomical Society of the Pacific Conference Series Vol. 485, Astronomical Data Analysis Software and Systems XXIII*. p. 391
- Denissenkov P. A., Herwig F., Truran J. W., Paxton B., 2013, *ApJ*, **772**, 37
- Denissenkov P. A., Truran J. W., Herwig F., Jones S., Paxton B., Nomoto K., Suzuki T., Toki H., 2015, *MNRAS*, **447**, 2696
- Dorman B., Rood R. T., O’Connell R. W., 1993, *ApJ*, **419**, 596
- Fink M., et al., 2014, *MNRAS*, **438**, 1762
- Fitzpatrick E. L., 1999, *PASP*, **111**, 63
- Flewelling H. A., et al., 2016, arXiv e-prints, [p. arXiv:1612.05243](https://arxiv.org/abs/1612.05243)
- Foley R. J., et al., 2013, *ApJ*, **767**, 57
- Fontaine G., Brassard P., Bergeron P., 2001, *PASP*, **113**, 409
- Freudling W., Romaniello M., Bramich D. M., Ballester P., Forchi V., García-Dabó C. E., Moehler S., Neeser M. J., 2013, *A&A*, **559**, A96
- Fuller J., Lai D., 2012, *MNRAS*, **421**, 426
- Gaia Collaboration et al., 2018, *A&A*, **616**, A1
- Geier S., et al., 2015, *Science*, **347**, 1126
- Giammichele N., Bergeron P., Dufour P., 2012, *ApJS*, **199**, 29
- Giclas H. L., Burnham R., Thomas N. G., 1970, *Lowell Observatory Bulletin*, **7**, 183
- Graur O., Bianco F. B., Modjaz M., Shivvers I., Filippenko A. V., Li W., Smith N., 2017, *ApJ*, **837**, 121
- Green G. M., et al., 2018, *MNRAS*, **478**, 651
- Heber U., 2016, *PASP*, **128**, 082001
- Hills J. G., 1983, *ApJ*, **267**, 322
- Hirsch H. A., Heber U., O’Toole S. J., Bresolin F., 2005, *A&A*, **444**, L61
- Hollands M. A., Koester D., Alekseev V., Herbert E. L., Gänsicke B. T., 2017, *MNRAS*, **467**, 4970
- Horne K., 1986, *PASP*, **98**, 609
- Huang Y., et al., 2016, *MNRAS*, **463**, 2623
- Isern J., Canal R., Labay J., 1991, *ApJ*, **372**, L83
- Istrate A. G., Marchant P., Tauris T. M., Langer N., Stancliffe R. J., Grassitelli L., 2016, *A&A*, **595**, A35
- Iwamoto K., Brachwitz F., Nomoto K., Kishimoto N., Umeda H., Hix W. R., Thielemann F.-K., 1999, *ApJS*, **125**, 439
- Jha S. W., 2017, *Type Iax Supernovae*. Springer International Publishing, Cham, pp 375–401, [doi:10.1007/978-3-319-21846-5_42](https://doi.org/10.1007/978-3-319-21846-5_42)
- John T. L., 1975a, *MNRAS*, **170**, 5
- John T. L., 1975b, *MNRAS*, **172**, 305
- John T. L., 1996, *MNRAS*, **279**, 859
- John T. L., Williams R. J., 1975, *MNRAS*, **171**, 7P
- Jones S., Röpké F. K., Pakmor R., Seitenzahl I. R., Ohlmann S. T., Edelmann P. V. F., 2016, *A&A*, **593**, A72
- Jones S., et al., 2019, *A&A*, **622**, A74
- Jordan IV G. C., Perets H. B., Fisher R. T., van Rossum D. R., 2012, *ApJ*, **761**, L23
- Justham S., Wolf C., Podsiadlowski P., Han Z., 2009, *A&A*, **493**, 1081
- Katsanis R. M., McGrath M. A., 1998, Technical report, The Calstis IRAF Calibration Tools for STIS Data. STScI
- Kausch W., et al., 2015, *A&A*, **576**, A78
- Kenyon S. J., Bromley B. C., Brown W. R., Geller M. J., 2014, *ApJ*, **793**, 122
- Kepler S. O., Koester D., Ourique G., 2016, *Science*, **352**, 67
- Kleinman S. J., et al., 2013, *ApJS*, **204**, 5
- Koester D., 2010, *Mem. Soc. Astron. Italiana*, **81**, 921
- Kromer M., et al., 2013, *MNRAS*, **429**, 2287
- Kromer M., et al., 2015, *MNRAS*, **450**, 3045
- Kupka F. G., Ryabchikova T. A., Piskunov N. E., Stempels H. C., Weiss W. W., 2000, *Baltic Astronomy*, **9**, 590
- Li W., et al., 2003, *PASP*, **115**, 453
- Li W., et al., 2011a, *MNRAS*, **412**, 1441
- Li W., Chornock R., Leaman J., Filippenko A. V., Poznanski D., Wang X., Ganeshalingam M., Mannucci F., 2011b, *MNRAS*, **412**, 1473
- Lisker T., Heber U., Napiwotzki R., Christlieb N., Han Z., Homeier D., Reimers D., 2005, *A&A*, **430**, 223
- Liu C.-N., 1999, PhD thesis, University of Nebraska - Lincoln, <https://search.proquest.com/docview/304512496?accountid=10755>
- Liu C.-N., Starace A. F., 1999, *Phys. Rev. A*, **59**, 3643
- Liu Z.-W., et al., 2013, *ApJ*, **774**, 37
- Luyten W. J., 1970, Proper Motion Survey with the forty-eight inch Schmidt telescope. The zone +70_ to +75_. Univ. Minnesota
- Lyman J. D., et al., 2018, *MNRAS*, **473**, 1359
- Mannucci F., Della Valle M., Panagia N., Cappellaro E., Cresci G., Maiolino R., Petrosian A., Turatto M., 2005, *A&A*, **433**, 807
- Mannucci F., Della Valle M., Panagia N., 2006, *MNRAS*, **370**, 773
- Maoz D., Mannucci F., Li W., Filippenko A. V., Della Valle M., Panagia N., 2011, *MNRAS*, **412**, 1508
- Maoz D., Mannucci F., Nelemans G., 2014, *A&ARv*, **52**, 107
- Marietta E., Burrows A., Fryxell B., 2000, *ApJS*, **128**, 615
- Marsh T. R., 1989, *PASP*, **101**, 1032
- Matteucci F., Raiteri C. M., Busson M., Gallino R., Gratton R., 1993, *A&A*, **272**, 421
- McMahon R. G., Banerji M., Gonzalez E., Koposov S. E., Bejar V. J., Lodieu N., Rebolo R., VHS Collaboration 2013, *The Messenger*, **154**, 35
- Minniti D., Saito R. K., Alonso-García J., Lucas P. W., Hempel M., 2011, *ApJ*, **733**, L43
- Moore C. E., 1959, A multiplet table of astrophysical interest. Part 1. NBS Technical Note, Washington: US Department of Commerce
- Morrissey P., et al., 2007, *ApJS*, **173**, 682
- Morton D. C., 2000, *ApJS*, **130**, 403
- Pan K.-C., Ricker P. M., Taam R. E., 2012, *ApJ*, **750**, 151
- Pelisolì I., Bell K. J., Kepler S. O., Koester D., 2019, *MNRAS*, **482**, 3831
- Phillips M. M., et al., 2007, *PASP*, **119**, 360
- Pickles A. J., 1998, *PASP*, **110**, 863
- Piffi T., et al., 2014, *A&A*, **562**, A91
- Raddi R., et al., 2017, *MNRAS*, **472**, 4173
- Raddi R., Hollands M. A., Gänsicke B. T., Townsley D. M., Hermes J. J., Gentile Fusillo N. P., Koester D., 2018a, *MNRAS*, **479**, L96
- Raddi R., Hollands M. A., Koester D., Gänsicke B. T., Gentile

- Fusillo N. P., Hermes J. J., Townsley D. M., 2018b, *ApJ*, **858**, 3
- Robinson E. J., Geltman S., 1967, *Phys. Rev.*, **153**, 4
- Ruiter A. J., Belczynski K., Fryer C., 2009, *ApJ*, **699**, 2026
- Ryabchikova T., Piskunov N., Kurucz R. L., Stempels H. C., Heiter U., Pakhomov Y., Barklem P. S., 2015, *Physica Scripta*, **90**, 054005
- Sale S. E., et al., 2010, *MNRAS*, **402**, 713
- Scannapieco E., Bildsten L., 2005, *ApJ*, **629**, L85
- Schlaflly E. F., Finkbeiner D. P., 2011, *ApJ*, **737**, 103
- Schlegel D. J., Finkbeiner D. P., Davis M., 1998, *ApJ*, **500**, 525
- Schönrich R., 2012, *MNRAS*, **427**, 274
- Schönrich R., Binney J., Dehnen W., 2010, *MNRAS*, **403**, 1829
- Schwab J., Rocha K. A., 2019, *ApJ*, **872**, 131
- Schwab J., Quataert E., Bildsten L., 2015, *MNRAS*, **453**, 1910
- Seitenzahl I. R., Townsley D. M., 2017, *Nucleosynthesis in Thermonuclear Supernovae*. Springer International Publishing, p. 1955, doi:10.1007/978-3-319-21846-5_87
- Seitenzahl I. R., Cescutti G., Röpke F. K., Ruiter A. J., Pakmor R., 2013, *A&A*, **559**, L5
- Shen K. J., Schwab J., 2017, *ApJ*, **834**, 180
- Shen K. J., Kasen D., Miles B. J., Townsley D. M., 2018a, *ApJ*, **854**, 52
- Shen K. J., et al., 2018b, *ApJ*, **865**, 15
- Smee S. A., et al., 2013, *AJ*, **146**, 32
- Smette A., et al., 2015, *A&A*, **576**, A77
- Tian H.-J., et al., 2017, *ApJS*, **232**, 4
- Travaglio C., Röpke F. K., Gallino R., Hillebrandt W., 2011, *ApJ*, **739**, 93
- Tremblay P.-E., Cummings J., Kalirai J. S., Gänsicke B. T., Gentile-Fusillo N., Raddi R., 2016, *MNRAS*, **461**, 2100
- Tremblay P.-E., et al., 2017, *MNRAS*, **465**, 2849
- Vallée J. P., 2008, *AJ*, **135**, 1301
- Vennes S., Nemeth P., Kawka J. R., Thorstensen J. R., Khalack V., Ferrario L., Alper E. H., 2017, *Science*, **357**, 680
- Vernet J., et al., 2011, *A&A*, **536**, A105
- Wang B., Han Z., 2009, *A&A*, **508**, L27
- Wang B., Han Z., 2012, *New Astron. Rev.*, **56**, 122
- Wang B., Meng X., Chen X., Han Z., 2009a, *MNRAS*, **395**, 847
- Wang B., Chen X., Meng X., Han Z., 2009b, *ApJ*, **701**, 1540
- Wang B., Justham S., Han Z., 2013, *A&A*, **559**, A94
- Wang B., Meng X., Liu D.-D., Liu Z.-W., Han Z., 2014, *ApJ*, **794**, L28
- Williams M. E. K., et al., 2013, *MNRAS*, **436**, 101
- Williams A. A., Belokurov V., Casey A. R., Evans N. W., 2017, *MNRAS*, **468**, 2359
- Wolf C., et al., 2018, *Publications of the Astronomical Society of Australia*, **35**, e010
- Wood M. A., 1995, in Koester D., Werner K., eds, *Lecture Notes in Physics*, Berlin Springer Verlag Vol. 443, White Dwarfs. p. 41, doi:10.1007/3-540-59157-5_171
- Woodgate B. E., et al., 1998, *PASP*, **110**, 1183
- Yamaguchi H., et al., 2015, *ApJ*, **801**, L31
- Zhang M., Fuller J., Schwab J., Foley R. J., 2019, *ApJ*, **872**, 29

This paper has been typeset from a \LaTeX file prepared by the author.